

1 **Acoustic emissions of nearly steady and uniform**
2 **granular flows: a proxy for flow dynamics and velocity**
3 **fluctuations**

4 **Bachelet, V.¹, Mangeney, A.^{1,2}, Toussaint, R.^{3,4}, de Rosny, J.⁵, Arran, M.I.^{1,6},**
5 **Farin, M.⁵, and Hibert, C.³**

6 ¹Université de Paris, Institut de Physique du Globe de Paris, CNRS, Paris, France

7 ²ANGE team, Inria, Lab. J.-L. Lions, CNRS, 75005, Paris, France

8 ³University of Strasbourg, CNRS, Institut Terre et Environnement de Strasbourg, UMR 7063, F-67084 ,

9 Strasbourg, France

10 ⁴PoreLab, Njord Centre, Department of Physics, University of Oslo, Oslo, Norway

11 ⁵Institut Langevin, ESPCI Paris, Université PSL, CNRS, 75005 Paris, France

12 ⁶LSRI, Campion Hall, University of Oxford, U.K.

13 **Key Points:**

- 14 • We analyze the high-frequency emissions and particle agitation of quasi-steady gran-
15 ular flows on constant slopes.
- 16 • Scaling laws between granular temperature, average velocity, shear rate and in-
17 ertial number are derived.
- 18 • A simple physical model for the acoustic emissions and acoustic efficiency of steady
19 flows is developed and tested.

Abstract

The seismic waves emitted during granular flows are generated by different sources: high frequencies by inter-particle collisions and low frequencies by global motion and large scale deformation. To unravel these different mechanisms, an experimental study has been performed on the seismic waves emitted by dry, dense, quasi-steady granular flows. The emitted seismic waves were recorded using shock accelerometers and the flow dynamics were captured with a fast camera. The mechanical characteristics of the particle collisions were analyzed, along with the intervals between collisions and the correlations in particles' motion. The high-frequency seismic waves (1-50 kHz) were found to originate from particle collisions and waves trapped in the flowing layer. The low-frequency waves (20-60 Hz) were generated by particles' oscillations along their trajectories, i.e. from cycles of dilation/compression during coherent shear. The profiles of granular temperature (i.e. the mean squared value of particle velocity fluctuations) and average velocity were measured and related to each other, then used in a simple steady granular flow model, in which the seismic signal consists of the variously attenuated contributions of shear-induced Hertzian collisions throughout the flow, to predict the rate at which seismic energy was emitted. Agreement with the measured seismic power was reasonable, and scaling laws relating the seismic power, the shear strain rate and the inertial number were derived. In particular, the emitted seismic power was observed to be approximately proportional to the root mean square velocity fluctuation to the power 3.1 ± 0.9 , with the latter related to the mean flow velocity.

Plain Language Summary

The generation of seismic waves during granular avalanches is studied experimentally and compared to simple models. The experiments allow granular layers to reach a steady state, waves are recorded through the basement with accelerometers and grain motion is followed with a fast camera. The origin of the different frequencies of signals is discussed. The role of the particles' collisions and the attenuation of the waves in the layer is investigated.

1 Introduction

Gravitational flows such as landslides, debris avalanches and rockfalls represent one of the major natural hazards threatening life and property in mountainous, volcanic, seis-

51 mic and coastal areas, with large events possibly displacing several hundred thousand
52 people. They play a key role in erosion processes on the Earth's surface. Gravitational
53 instabilities are also closely related to volcanic, seismic and climatic activity and thus
54 represent potential precursors or proxies for changes in these activities with time, as shown
55 for example for the Piton de la Fournaise volcano, Réunion [Durand et al., 2018, Hib-
56 ert et al., 2014, 2017a] or for the Soufrière Hills volcano, Montserrat [Calder et al., 2005,
57 Levy et al., 2015].

58 Research involving the dynamic analysis of gravitational mass flows is advancing
59 rapidly. One of its ultimate goals is to produce tools for detecting natural instabilities
60 and for predicting the velocity, dynamic pressure and runout extent of rapid landslides.
61 However, the theoretical description and physical understanding of these processes in a
62 natural environment are still open and extremely challenging problems [see Delannay et
63 al. [2017] for a review]. In particular, the origin of the high mobility of large landslides
64 is still unexplained, with different hypotheses proposed in the literature (acoustic flu-
65 idization, flash heating, etc.) [Lucas et al., 2014]. The lack of field measurements rele-
66 vant to the dynamics of natural landslides prevents us from fully understanding the pro-
67 cesses involved and from predicting landslide dynamics and deposition. Indeed, these events
68 are generally unpredictable, but have a strongly destructive power. Furthermore, data
69 on the deposits are not always available due to subsequent flows, erosion processes or site
70 inaccessibility.

71 In this context, analysis of the seismic signal generated by natural instabilities pro-
72 vides a unique way to detect and characterize these events and to discriminate between
73 the physical processes involved. When flowing down the slope, landslides generate seis-
74 mic waves in a wide frequency range that are recorded by local, regional or global seis-
75 mic networks, depending on the event size [Allstadt et al., 2018, Okal, 1990]. As a re-
76 sult, the recorded seismic signal, with frequencies ranging from about 0.006 Hz to 30 Hz,
77 carries key information on landslide dynamics to distances far from the source. However,
78 the characterization of landslides from their seismic signals suffers from uncertainty about
79 the respective effects on such signals of mean flow dynamics, grain-scale processes, to-
80 pographic variation, and wave propagation. It is commonly speculated that grain im-
81 pacts on the substrate generate high frequencies (> 1 Hz in geophysical contexts), while
82 the mean flow acceleration/deceleration is responsible for lower frequencies.

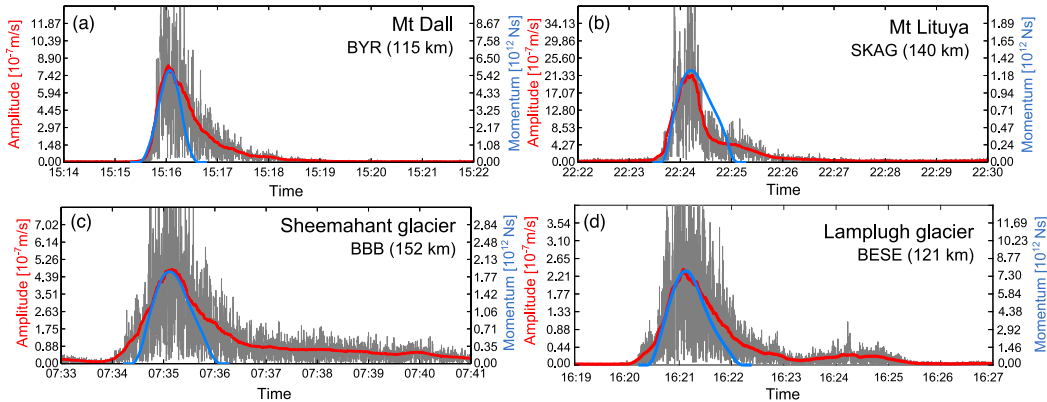


Figure 1. Seismic signal envelope (gray), smoothed envelope (red) and inverted momentum (blue) from the inversion method proposed by Ekström & Stark [2013] for landslides on a) Mt Dall, b) Mt Lituya, c) the Sheemahant glacier and d) the Lamplugh glacier, with the second line of each legend indicating the seismic station and its distance from the landslide.

Much work has been devoted to extracting information on geophysical flow dynamics from low-frequency signals (periods $10 \text{ s} < \tau < 120 \text{ s}$), with the net force that a landslide applies to the ground recovered using signal deconvolution, e.g. Allstadt [2013], Ekström & Stark [2013], Hibert et al. [2017b], Kanamori & Given [1982], La Rocca et al. [2004], Lin et al. [2010], Moretti et al. [2012], Yamada et al. [2013], Zhao et al. [2015]. The time history of this force is directly related to the acceleration and deceleration of the flow along the topography. Comparing this force with the force simulated with landslide models makes it possible to recover a landslide’s characteristics and dynamics, such as its volume and timing, the friction coefficients involved, the role of erosion processes, and the underlying ground’s composition (rock or ice) and topography [Favreau et al., 2010, Moretti et al., 2020, 2015, 2012, Schneider et al., 2010, Yamada et al., 2018, 2016].

The high-frequency signal is much more difficult to interpret, due in part to the strong effect of topography and Earth heterogeneity along seismic waves’ path from source to receiver [Kuehnert et al., 2020, 2021]. For this reason, mainly empirical relationships have been proposed between high-frequency signals and landslide characteristics [Allstadt et al., 2020, Dammeier et al., 2011, Deparis et al., 2008, Norris, 1994]. However, high-frequency signals are recorded more commonly than low-frequency signals, because of the lower price of short period seismometers and because small landslides (with volumes $< 10^7 \text{ m}^3$ [Allstadt et al., 2018]) only generate frequencies larger than about 1 Hz.

106 Recent studies show correlations between the high-frequency signal (energy, envelope,
107 etc.) and the mean properties of the flow (potential energy lost, force, velocity, momen-
108 tum, etc.) estimated using landslide models [Hibert et al., 2014, 2011, Levy et al., 2015]
109 or from inversion of low-frequency seismic data [Hibert et al., 2017b]. In particular, Hi-
110 bert et al. [2017b] observed that the flow momentum is generally proportional to the am-
111 plitude of the high-frequency envelope of the signal. . Even non-accelerating, constant-
112 velocity flows generate seismic waves, possibly due to grain agitation.

113 The generation of high-frequency signals by agitated flowing grains has been both
114 observed and theorized. Huang et al. [2007] compared the high-frequency seismic sig-
115 nals generated by rock impacts and debris flows (grain/fluid mixtures) and concluded
116 that one of the main sources of ground vibration caused by debris flows is the interac-
117 tion of rocks or boulders with the channel bed. Models for this process have been both
118 developed and tested, by Farin, Tsai, et al. [2019], Kean et al. [2015], Lai et al. [2018],
119 Zhang et al. [2021]. However, the complexity of natural landslides and the difficulty of
120 obtaining accurate measurements of their dynamics makes it nearly impossible to quan-
121 tify, or rigorously test models of, the link between grain-scale physical processes, such
122 as velocity fluctuations, and the generated seismic signal. More generally, the measure-
123 ment of particle agitation, called granular temperature in the kinetic theory of granu-
124 lar flows, and its link with mean flow properties in dense flows, are still open questions,
125 closely related to the rheology of granular materials [see e.g. Andreotti et al. [2013], De-
126 lannay et al. [2017] for review papers].

127 A few studies addressed this issue with laboratory scale experiments, recording and
128 quantifying the seismic (i.e. acoustic) waves generated by almost steady and uniform gran-
129 ular flows. These experiments make it possible to test physical interpretations of the char-
130 acteristics of the seismic signal generated by natural landslides and to quantify the par-
131 tition of energy between the flow and its seismic emissions. Furthermore, such experi-
132 ments provide a unique way to check models of granular flows and seismic wave gener-
133 ation in a simple configuration, before tackling natural applications.

134 In a 8-meter long channel, Huang et al. [2004] investigated the acoustic waves gener-
135 ated by i) the friction and impacts of rocks of about 100 g to 1 kg on a granular bed
136 filled with water and slurry and ii) debris flows of gravel and water/slurry. They recorded
137 similar frequencies for individual rock motion and debris flows, as observed in the field

138 by Huang et al. [2007]. Their measurements also showed that the amplitude of the acous-
139 tic signal increases with gravel size. However, as with the later, better-instrumented ex-
140 periments of de Haas et al. [2021] on debris flows of clay, sand, gravel and water, the com-
141 plexity of the materials involved and the lack of measurements at the grain scale made
142 it difficult to capture the origin of the generated signal and to quantify the link between
143 the acoustic measurements and the flow properties.

144 Working with more monodisperse grains, researchers investigating “booming dunes”
145 have recorded acoustic signals that are generated by grain agitation, but differ from those
146 of landslides in being coherent. The reviews of Hunt & Vriend [2010] and Andreotti [2012]
147 present different perspectives on experiments and field observations, agreeing that in-
148 ternal shear generates initial signals with frequency related to the shear rate, but with-
149 out consensus on the mechanism by which certain dune sands produce clear tones of around
150 100 Hz. In sheared and confined granular layers of similarly monodisperse grains, wave
151 propagation through the granular structure has been investigated by Lherminier et al.
152 [2014].

153 Shearing similarly well-sorted beach sands in a torsional rheometer, Taylor & Brod-
154 sky [2017] found that the square of the acceleration measured with their accelerometers
155 divided by the number of particles was proportional to $I \times d^3$, where d is the particle
156 diameter and I the so-called inertial number, defined as the ratio between the time scale
157 related to shear and the time scale related to particle rearrangement under confining pres-
158 sure. However, Taylor & Brodsky [2017] neither calculated absolute values of the acous-
159 tic energy nor measured the characteristics of the flow such as velocity fluctuations, mean
160 velocity profiles, etc.

161 A series of experiments on granular impacts on various smooth beds showed that
162 Hertz theory quantitatively explains the acoustic signal generated in the bed substrate
163 [Farin et al., 2015]. These experiments also showed that power laws issued from this the-
164 ory make it possible to empirically relate the acoustic energy to the properties of the im-
165 pactor (mass, velocity) on smooth, rough and erodible beds [Bachelet et al., 2018, Farin
166 et al., 2016, 2015]. More specifically, the characteristic frequency of the acoustic sig-
167 nal is shown to decrease with increasing impactor mass and to increase with increasing
168 impact velocity, while the radiated energy of the acoustic signal increases with both in-
169 creasing mass and increasing velocity, as observed for debris flows [Okuda et al., 1980]

170 and for single block rockfalls [Hibert et al., 2017c]. These quantitative relationships, be-
171 tween acoustic and kinematic properties, were discovered thanks to accurate measure-
172 ment and calculation both of grain motion and of the absolute value of radiated acous-
173 tic energy, using coupled optical and acoustic methods.

174 With similar methods, Farin et al. [2018, 2019] showed that, during 3D granular
175 collapses on inclined planes, the rate of seismic energy emission varies in the same man-
176 ner as the flow velocity. In particular, analysing the period of flow that follows grains’
177 initial acceleration and deceleration, the rate of seismic energy emission increases with
178 increasing slope, as do the downslope velocity and the agitation of particles at the flow
179 front. However, grain-scale fluctuations were not measured.

180 The acoustic signals of flows that are comparably energetic, but steady and appar-
181 ently uniform, were investigated by Arran et al. [2021], which used carefully calibrated
182 force and flux measurements, high-speed photography and accelerometer recordings to
183 test the models of Farin, Tsai, et al. [2019], Kean et al. [2015], Lai et al. [2018]. With
184 the flows’ bulk inertial numbers I between 0.1 and 5 and indications of basal slip, acous-
185 tic signals were best predicted by a model adapted from Farin, Tsai, et al. [2019], in which
186 signals are generated by Hertzian impacts, with the ground, of particles with mean ve-
187 locity equal to that of the flow. But this prompts a new question: how are signals gen-
188 erated by less energetic flows, in which basal particles are almost static and the collisions
189 of other particles, far from the flow’s base, will be more significant?

190 We investigate here the quantitative link between velocity fluctuations, mean flow
191 properties and acoustic energy, by combining accurate optical and acoustic measurements
192 of granular flows over a range of slopes. Compared to Arran et al. [2021], we focus here
193 on more gentle slopes, on which flows are almost steady and uniform but a persistent
194 contact network links almost static basal particles to energetic particles far from the base.
195 Our objectives are to: (1) capture and quantify the fluctuations and heterogeneities in
196 almost steady uniform flows and their relationship with mean flow properties, (2) char-
197 acterize and quantify the radiated acoustic energy, (3) relate the acoustic characteris-
198 tics (energy, frequency) to the grain-scale and mean properties of the flow, (4) check whether
199 a simple model based on particle collisions at fluctuating velocities can quantitatively
200 explain the measured seismic power, (5) quantify the relative contributions of collisions
201 within the flow and with the bed on the generated acoustic energy, (6) quantify the pro-

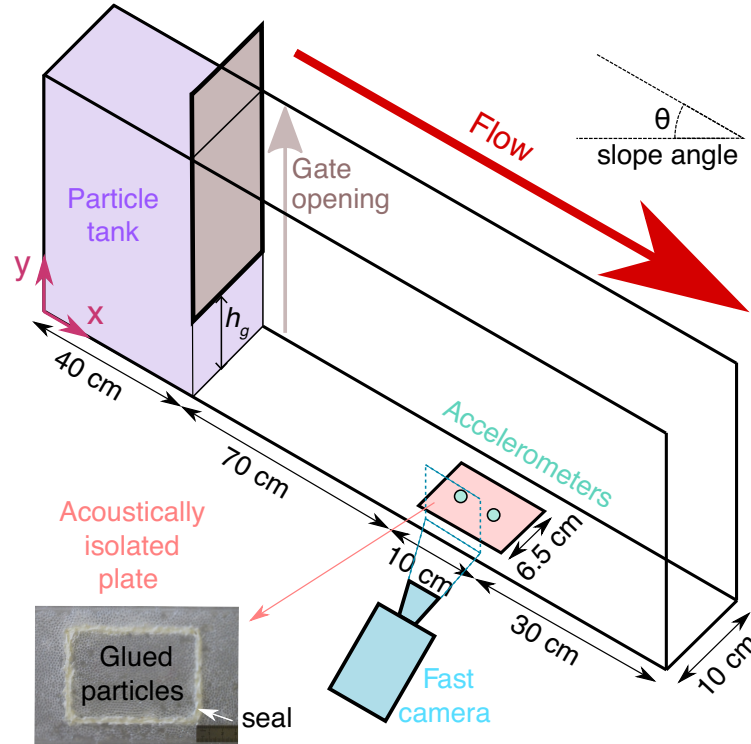
202 portion of energy lost by vibrations and (7) discuss our results with regards to field ob-
 203 servations.

204 **2 Set-up**

205 The experimental set-up consists of a 1.5 m long chute made of poly(methyl methacry-
 206 late) (PMMA), inclined at an angle θ to the horizontal, with rigid side walls 10 cm apart.
 207 Granular flows are initiated by opening a gate that releases glass particles of diameter
 208 $d = 2$ mm and density $\rho = 2500$ kg m⁻³, initially stored in a tank (Fig. 2). The rough
 209 bed is made of the same glass particles, glued to the PMMA plate with phenyl salicy-
 210 late, a crystalline substance with low melting point. As opposed to tape, it prevents the
 211 glued particles from vibrating and significantly disturbing the acoustic signal. The two
 212 control parameters are the height of the gate h_g and the slope angle of the channel θ ,
 213 which varies between $\theta = 16.5^\circ$ and $\theta = 18.1^\circ$. Note that the flow thickness is related
 214 but not equal to the height of the gate, which varies between $h_g = 4.4$ cm and $h_g =$
 215 8.5 cm. In this range of inclination angles, almost steady and uniform flows can be ob-
 216 served at about 70 cm from the gate (as discussed below). The characteristics of these
 217 flows are summarized in Table 1. 70 cm from the gate, a Photron SA5[®] high-speed cam-
 218 era (5000 frames per second) records the flow during 2 s with a field of view of around
 219 50 mm by 50 mm. Simultaneously, two accelerometers (*Bruel & Kjaer*, 8309, bandwidth
 220 10 Hz-54 kHz) record the radiated acoustic waves. These accelerometers are glued, us-
 221 ing the same phenyl salicylate as for the particles of the rough surface, on the back of
 222 a $L \times l = 10$ cm \times 6.4 cm plate, isolated acoustically from the rest of the channel bot-
 223 tom. To isolate the plate, we fixed it to the channel bottom with a silicone sealant (see
 224 bottom of Fig. 2).

235 **3 Optical and Acoustic Methods**

236 Our objective is to obtain deep quantitative insights into the mean properties of
 237 the flow and into its fluctuations and heterogeneity, in order to further interpret the gen-
 238 erated acoustic signal in terms of grain scale and mean flow dynamics. Before analysis
 239 of these measurements, in section 4, let us detail below the optical and acoustic meth-
 240 ods used here to measure flow and acoustic characteristics, respectively. To illustrate the
 241 methods, we focus in this section on the two ‘extreme’ cases representing the slower flows
 242 by experiments 1 and 2, at $\theta = 16.5^\circ$, with flow thicknesses $h = 3.5$ cm and $h = 3.6$ cm



230 **Figure 2.** Set-up, composed of a narrow inclined channel in which granular flows are created
 231 by opening the gate of the upstream tank that contains glass particles. The same particles are
 232 glued to the bottom plate to obtain a rough surface. The flow properties are measured using
 233 a high-speed camera and the generated acoustic waves by accelerometers fixed on the channel
 234 bottom.

225 **Table 1.** Parameters of the quasi-steady and quasi-uniform flows obtained in our 9 experiments
 226 (referred to by the index 1-9): slope angle of the channel θ , thickness of the flow h , downslope
 227 velocity of the surface particles V_{xs} , depth- and time-averaged downslope velocity $\langle\langle V_x \rangle\rangle$, shear
 228 rate $\langle\dot{\gamma}\rangle$ and inertial number $\langle I \rangle$. Note that here $d = 2$ mm, $\sqrt{gd} \simeq 0.14$ m/s and $\sqrt{d/g} \simeq 0.014$
 229 s.

Index	$\theta [^\circ] (\pm 0.1)$	$h/d (\pm 0.5)$	$V_{xs}/\sqrt{gd} (\pm 0.05)$	$\langle\langle V_x \rangle\rangle/\sqrt{gd} (\pm 0.05)$	$\sqrt{d/g} \langle\dot{\gamma}\rangle (\pm 0.01)$	$\langle I \rangle (\pm 0.003)$
1	16.5	17.5	2.15	0.65	0.12	0.070
2	16.5	18.0	2.05	0.55	0.10	0.054
3	16.5	20.0	2.35	0.80	0.12	0.061
4	17.2	15.5	2.50	0.75	0.15	0.094
5	17.2	16.5	2.85	0.90	0.16	0.094
6	17.2	16.5	2.95	1.00	0.17	0.103
7	18.1	14.5	2.02	0.50	0.11	0.074
8	18.1	15.0	2.95	0.90	0.18	0.103
9	18.1	16.5	3.45	1.10	0.21	0.131

243 and surface velocities $V_{xs} = 0.30$ m s⁻¹ and $V_{xs} = 0.29$ m s⁻¹, and the faster flows by
 244 experiment 9 at $\theta = 18.1^\circ$, with $h = 3.3$ cm and $V_{xs} = 0.48$ m s⁻¹ (Table 1).

245 3.1 Flow Measurement using Optical Methods

246 The flows in all our experiments reach an almost steady and uniform regime: their
 247 heights typically vary by one particle diameter or less in space and time over the entire
 248 recorded experiment (see Fig. A1 in the Appendix). The flow is steady over the central
 249 half of the experiment, up to statistical fluctuations. From the average height decrease
 250 between $x = 0$ and $x = 25d = 50$ mm, (Fig. A1 c in the Appendix), a variation from
 251 uniformity of 1° can be estimated: the slope angle is slightly below that required to main-
 252 tain a steady, uniform flow, and steadiness is maintained by net energy input from the
 253 grains' initial release.

3.1.1 Mean Velocity and Fluctuations

We measured particle velocities $\mathbf{V} = (V_x, V_y)$ by Correlation Image Velocimetry (CIV) and Particle Tracking Velocimetry (PTV). CIV divides each image from the high-speed camera into boxes and calculates the average displacement into each box by correlation of the graymap between successive images (Fig. 3a). The size of the boxes is a crucial parameter. Boxes that are too large miss individual particles whereas boxes that are too narrow do not allow good correlations. Similarly to Gollin et al. [2015a], the size of the boxes was chosen to be equal to 1.14 particles. The overlap between boxes is 75%. We used the code developed by Thielicke & Stamhuis [2014].

On the other hand, PTV detects and follows the particle positions, making it possible to record their trajectories (Fig. 3b). The particles are semi-transparent and cause complex reflection effects. Consequently, a compromise must be made between the completeness and accuracy of detections. PTV shows that particles are essentially organized into layers that do not really mix during the flow. Mean velocities $\langle \mathbf{V} \rangle = (\langle V_x \rangle, \langle V_y \rangle)$ are therefore calculated by averaging the measurements within each layer (over 1 particle diameter in the y -direction), the borders of which are clearly visible on the PTV images (Fig. 3b). As done for calculating the mean thickness, the averaging is performed over about 16 particles in space in the downslope direction and over the whole experiment duration (2 s).

Velocity fluctuations δV are computed over the same intervals (2 s, 16 particles in the x -direction and 1 particle in the y -direction) by taking the standard deviation of the norm of the velocities:

$$\delta V = \sqrt{\delta V_x^2 + \delta V_y^2}, \quad (1)$$

where $\delta V_i^2 = \langle (V_i - \langle V_i \rangle)^2 \rangle$ the variance of the velocity along the i -direction, with $i = x, y$. For granular systems, the measurement of velocity fluctuations may lead to scale dependency effects due to gradients developing in the flow (see e.g. Artoni & Richard [2015a]). Indeed, the thickness w of the layers within which the velocity fluctuations are calculated affects the estimates. Following Glasser & Goldhirsch [2001], we showed that the size dependency starts for $w > 2d$ (see Fig. B1 of Appendix B). In the following, we will consider velocity fluctuations calculated with a window size $w = d$. Note that when velocity fluctuations are calculated with a smaller averaging window (e.g. $w = 0.2d$), the layering of the flow clearly appears and resembles that observed by Weinhart et al.

[2013] (Fig. B1, Appendix B). Note also that velocity fluctuations of about $0.1\sqrt{gd}$ are measured near the bottom, where the mean velocity is zero. This indicates the order of magnitude of the error in the measurement of velocity fluctuations ($\sim 0.01 \text{ m s}^{-1}$).

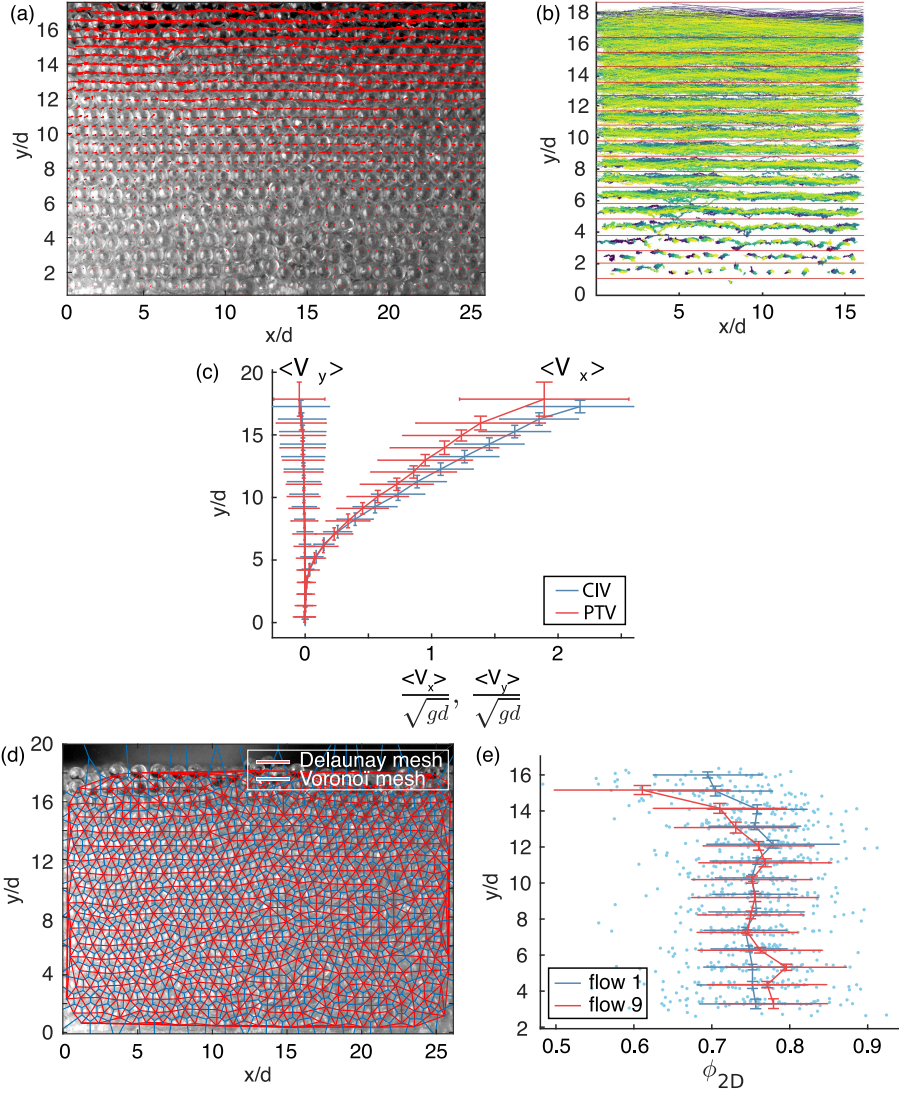
The profiles of mean velocity, in both the downslope ($\langle V_x \rangle$) and normal ($\langle V_y \rangle$) directions, differ by at most 10% when obtained using CIV as compared to PTV, as illustrated in Fig. 3c. In contrast, velocity fluctuations may differ by up to a factor of two between the two methods. This discrepancy has also been observed by Gollin et al. [2015b] and Gollin et al. [2017] and seems to be due to the average nature of CIV, which is therefore less suitable to measure fluctuations. As a result, PTV measurements will be used in the following, as in Pouliquen [2004], except for mapping of the spatio-temporal distribution of velocity fluctuations (Fig. C1).

3.1.2 *Packing Volume Fraction*

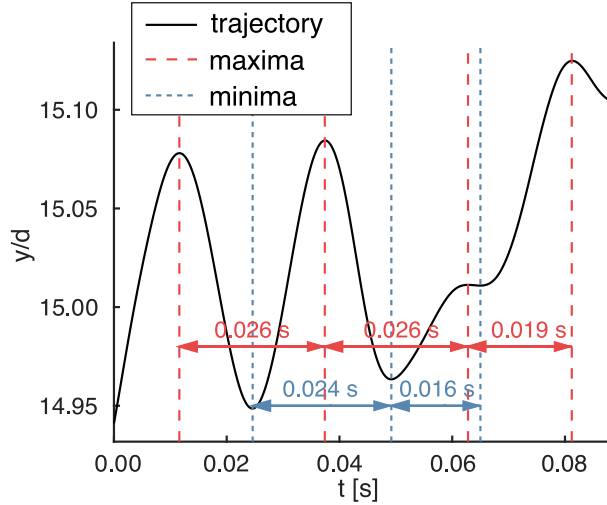
The set-up can only measure the surface packing fraction ϕ_{2D} at the lateral walls (Fig. 3de), with specular reflections making it impossible to apply Sarno et al. [2016]’s method for estimating the (typically smaller) volume packing fraction. Furthermore, one observes an ordering of the particles along the walls, with a close to hexagonal pattern visible in Fig. 3d. Nevertheless, one expects qualitative variations with depth of the 2D volume fraction along the walls to reflect the qualitative behavior in the volume: as is typically observed, we measure an almost constant packing fraction within the flow and a decrease when approaching the free surface (Fig. 3e). Due to the strong uncertainty in our measurements, the change of ϕ_{2D} when increasing the slope angle (i.e. when the inertial number changes) is hard to capture, even though a decrease of ϕ_{2D} with increasing inertial number is visible near the surface, in agreement with the literature [GDR MiDi, 2004]. Calculation of the volume fraction shows the layering of the granular flows observed for example by Artoni & Richard [2015a] and Weinhart et al. [2013].

3.1.3 *Frequency of Particle Oscillations*

During the flow, vertical oscillations of the particles can be observed, related to compression/dilatation effects occurring when one layer passes over another (see Movies 1 and 2 in supplementary material). These oscillations are captured in PTV measurements of the trajectories of particles located at the surface (Fig. 4). Indeed, several oscillations



296 **Figure 3.** Examples, from experiment 2, of image analysis. (a) A velocity field calculated by
 297 CIV (red arrows) and (b) a superposition of particle trajectories, over 2 s, obtained with PTV.
 298 The organization of the flow into a superposition of layers is clearly visible. In (b), red lines indi-
 299 cate the separation between layers. (c) Mean downslope and normal velocity profiles $\langle V_x \rangle$ and
 300 $\langle V_y \rangle$, as a function of the position above the bottom y . The associated velocity fluctuations are
 301 represented by the horizontal error bars. Vertical error bars correspond to the thickness of the
 302 layer within which the velocity has been averaged. One can compare the measurements made by
 303 CIV (blue line) and PTV (red line). (d) and (e) Surface packing fraction of the particles in con-
 304 tact with the lateral wall: (d) manual picking of the particles of flow 1 ($\theta = 16.5^\circ$, $h/d = 17.5$, i.e.
 305 $h = 35$ mm) at one instant and (e) the inferred surface packing fraction (blue dot) per Voronoi
 306 cell. The average values are plotted in the solid blue line. For comparison, the average surface
 307 packing fractions of flow 9 ($\theta = 18.1^\circ$, $h/d = 16.5$, i.e. $h = 33$ mm) are plotted with the solid red
 308 line.



341 **Figure 4.** Example (from experiment 2) of vertical particle oscillations captured by PTV, for
 342 a particle located close to the surface of the flow: The smoothed trajectory demonstrates the
 343 calculation of the average period of the oscillations $\tau \simeq 0.02$ s.

328 can be observed before these particles' relatively high velocity causes their tracking to
 329 fail. On the contrary, for particles located deeper in the flow, oscillations generally oc-
 330 cur when tracking has already failed. For oscillations that are captured, the oscillation
 331 frequency f_{osc} is calculated by filtering each particle trajectory with two filters and tak-
 332 ing the median of values $1/\tau_i$, where each $\tau_i \simeq 0.02$ s is the time between successive max-
 333 ima or minima of each filtered trajectory (Fig. 4). More precisely, the first filter is a nor-
 334 malized median filter adapted from Westerweel & Scarano [2005] and applied to each tra-
 335 jectory component, with a neighborhood radius of 5 successive positions, an acceptable
 336 fluctuation level of $\varepsilon = 0.10$ pixels and a detection threshold equal to the median dif-
 337 ference between particles' velocities and the median of velocities in their local neighbor-
 338 hood (for technical details, see Westerweel & Scarano [2005]). The second filter is a sec-
 339 ond order zero-phase low pass filter (cut-off frequency of 50 Hz). The median filter has
 340 been chosen to suppress random fluctuations.

344 3.2 Elastic Wave Measurements

345 The elastic waves generated by the granular flows and by their interactions with
 346 the bottom are recorded by two accelerometers glued to the isolated plate (Fig. 5a). It
 347 is assumed here that the accelerometers mainly record the vibrations generated by the

348 section of granular flow over the plate. Isolation of the plate from the rest of the flume
 349 was verified by comparing the signals recorded by accelerometers glued to these two el-
 350 ements [Bachelet, 2018].

351 Regarding the terminology in this work, we monitor the elastic (mechanical) waves
 352 transmitted to the solid plate under the flow. They arise due to the motion of the flow-
 353 ing grains, and are transmitted to the plate mostly by the grains in contact with the plate.
 354 Some conversion of waves transmitted in the air to waves transmitted in the grains or
 355 plate is also possible, but any such converted waves are presumably small in amplitude
 356 compared to the waves transmitted entirely via the solid grains. Concerning the termi-
 357 nology, researchers in the acoustic community use the term “acoustic wave” for all me-
 358 chanical waves, whether in gas, solid or liquid. Researchers in geophysics and seismol-
 359 ogy use the term “acoustic wave” for waves propagating in a gas or liquid, and “seismic
 360 wave” for waves in a solid. Most articles studying waves in solids generated during gran-
 361 ular flow term them “acoustic”, without distinction of the propagation medium, and most
 362 articles studying waves generated at field scale by avalanches or debris flow term them
 363 “seismic”. Hence, we adopt this terminology, and will refer to the monitored waves as
 364 acoustic waves or elastic waves at the laboratory scale, and seismic waves at the field scale.

365 **3.2.1 Radiated Elastic Power**

366 The average radiated elastic power over duration Δt is $\Pi_{el} = W_{el}/\Delta t$, where W_{el}
 367 is the radiated elastic energy. The acoustically isolated plate is small compared to the
 368 characteristic viscoelastic attenuation length of energy in PMMA. As a result, elastic waves
 369 are reflected many times at the boundaries of the plate, leading to a diffuse elastic field,
 370 i.e. a situation in which energy can be assumed to be homogeneously distributed over
 371 the plate and equipartitioned. The elastic energy dissipated over Δt can then be approx-
 372 imated from measurements of plate-normal velocity v_z , by using the diffuse field theory
 373 proposed by Farin et al. [2016]:

$$W_{el} = M \gamma_p v_g \times \int_{\Delta t} v_z^2(t) dt, \quad (2)$$

374 where $M \simeq 80$ g is the mass of the isolated piece of plate, $\gamma_p \simeq 3$ m⁻¹ its average vis-
 375 coelastic attenuation and $v_g \simeq 1000$ m s⁻¹ the average group velocity of the radiated
 376 acoustic waves (A_0 Lamb waves). The value of γ_p is obtained by measuring the response
 377 of the plate at various distances with a source and a vibrometer and the value of v_g by

378 calculating the dispersion relation of the A_0 Lamb modes of the plate, following Royer
 379 & Dieulesaint [2000] [Bachelet, 2018]. The measurements to determine γ_p were performed
 380 on a PMMA plate of size 1 m by 1 m, with material and thickness corresponding to the
 381 isolated piece of plate. The amplitude at first passage of a wave induced by a piezoelec-
 382 tric sensor was measured with the vibrometer at distances up to 60 cm from the source,
 383 every mm. The source was excited by a 1 s-long chirp (or sweep) with an instantaneous
 384 frequency linearly increasing from 1 kHz to 50 kHz. This permitted determination of the
 385 dispersion relationship and the attenuation of the A_0 mode in both the 1 m by 1 m plate
 386 and the experimental isolated plate. A large time window $\Delta t = 0.2$ s is selected in or-
 387 der to consider only slow changes of Π_{el} . The fast fluctuations will be characterized in
 388 the next section. An example of radiated elastic power computation is presented in Fig.
 389 5a.

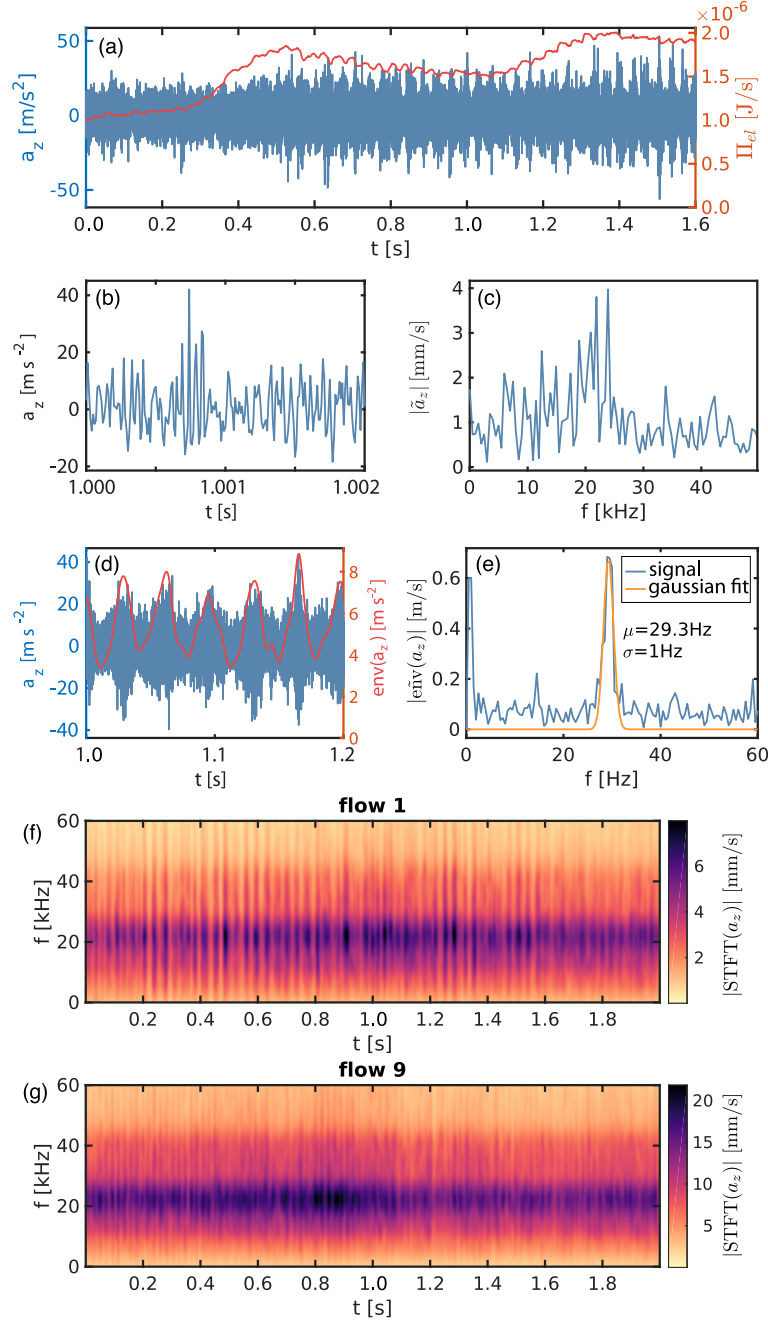
390 **3.2.2 Frequency Content**

391 The spectrograms shown in Fig. 5f-g indicate that the main frequency content of
 392 the acoustic signals lies between 20 and 30 kHz. Amplitude spectra are not studied be-
 393 yond 54 kHz, which is the upper limit of the accelerometers' flat response. This prevents
 394 us from reliably measuring the mean frequencies of the seismic signals.

395 Vertical stripes can be identified on the spectrograms (Fig. 5f,g). The time inter-
 396 val between these stripes decreases as the slope angle increases. The frequency content
 397 of this amplitude modulation is between 25 and 50 Hz, i.e., about 1000 times smaller than
 398 the highest frequencies at which we detect signals. To calculate the modulation frequency
 399 f_{mod} , we first extract the envelope of the signal (the absolute value of its analytic rep-
 400 resentation) and apply a low pass filter (cut-off frequency empirically fixed at 75 Hz). Then,
 401 the modulation frequency is determined by fitting a Gaussian in Fourier space (Fig. 5d,e).

407 **4 Flow Characteristics**

408 Our objective here is to capture the relationship between mean flow properties and
 409 the fluctuations that are expected to play a role in acoustic emissions. Note that the flow
 410 measurements are made at the side walls. It is well known that the wall boundaries sig-
 411 nificantly affect the mean flow quantities and their fluctuations, as will be discussed be-



402 **Figure 5.** Acoustic signal of flow number 2: (a) acceleration of the vibration (blue) and
 403 associated elastic power (red), (b) an excerpt of the acoustic signal and (c) its frequency spec-
 404 trum, (d) envelope (red) of the acoustic signal (blue) and (e) the frequency spectrum of this
 405 envelope. (f) and (g) Spectrograms of the signal of (f) experiment 1 ($\theta = 16.5^\circ$, $h = 3.5$ cm,
 406 $V_{xs} = 0.30$ m s⁻¹) and (g) experiment 9 ($\theta = 18.1^\circ$, $h = 3.3$ cm, $V_{xs} = 0.48$ m s⁻¹).

412 low (see e.g. Artoni & Richard [2015b], Fernández-Nieto et al. [2018], Jop et al. [2005,
413 2007], Mandal & Khakhar [2017], Taberlet et al. [2003]).

414 **4.1 Mean Flow**

415 The nearly uniform and steady flows obtained here, confined in a narrow channel
416 inclined at slope angles between 16.5° and 18.1° , are similar to those observed by Hanes
417 & Walton [2000] in similar settings. In these flows, the mean downslope velocity $\langle V_x \rangle(y)$
418 is maximized at the free surface, decreasing down to zero near the bottom (Fig. 6). Such
419 convex velocity profiles are observed in flows confined in narrow channels (see e.g. An-
420 cey [2001], Courrech du Pont et al. [2003], Jop et al. [2005, 2007], Mandal & Khakhar
421 [2017], GDR MiDi [2004], Taberlet et al. [2003]) and differ from the Bagnold-like veloc-
422 ity profiles obtained for steady and uniform flows in wide channels (see GDR MiDi [2004]
423 or Fig. 4 of Fernández-Nieto et al. [2018]). These profiles have a shape that can be ap-
424 proximately fitted by the velocity profiles assumed in Josserand et al. [2004] to describe
425 heap flows:

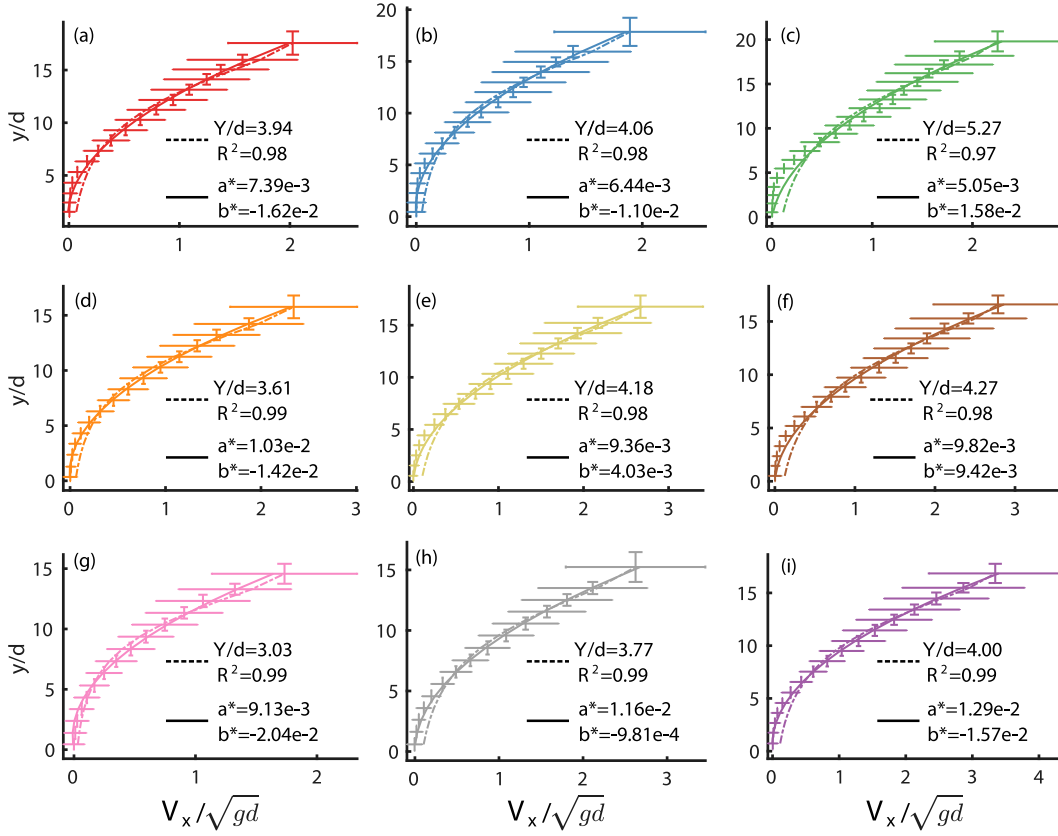
$$1 - \frac{\langle V_x^J \rangle(y')}{\langle V_x \rangle(y' = 0)} = \left(\frac{1 - e^{-y'/Y}}{1 + (\frac{\phi_M}{\phi_m} - 1)e^{-y'/Y}} \right)^{3/2}, \quad (3)$$

426 where $y' = h - y$ and h is the height of the flow surface, Y is a fitting parameter, and
427 $\phi_m = 0.5$ and $\phi_M = 0.65$ are the loose and dense random packing fraction, respec-
428 tively. Fig. 6 shows that Eq. (3) fits our experimental data quite well, except near the
429 bottom for experiments with thick flow depth h , for which the horizontal velocity is non-
430 zero at the base. While second order polynomials ($\langle V_x \rangle / \sqrt{gd} = a^*(y/d)^2 + b^*(y/d)$)
431 give even better results, especially near the bottom, we use the physically motivated fits
432 of equation (3) to calculate the shear strain rate $\dot{\gamma} = \partial \langle V_x^J \rangle / \partial y$. We do not calculate
433 γ for the surficial layer, which is poorly modelled by dense, continuum shear.

439 The shear strain rate $\dot{\gamma}$ decreases from the surface down to the bottom (Fig. 7b).
440 Granular flows are characterized by the inertial number $I = \dot{\gamma}d / \sqrt{P/\rho}$, where ρ is the
441 grain density and P the pressure, taken here to be hydrostatic ($P = \rho\phi g \cos(\theta)(h -$
442 $y)$):

$$I(y) = \frac{\dot{\gamma}(y)d}{\sqrt{\phi g \cos(\theta)(h - y)}}. \quad (4)$$

443 The packing fraction is approximated by $\phi = 0.6$ [Jop et al., 2005] because we do not
444 have access to the packing fraction in the bulk of the flow (see section 3.1.2). As the ve-



434 **Figure 6.** Velocity profiles of all the experiments, with letters (a) to (i) referring to flows
 435 1 to 9, corresponding to the angles (a-c) $\theta = 16.5^\circ$, (d-f) $\theta = 17.2^\circ$ and (g-i) $\theta = 18.1^\circ$
 436 and to increasing flow thickness along each row (see Table 1 for details). Two theoretical pro-
 437 files have been fitted: the ones given by Eq. (3) in dashed lines and a 2nd order polynomial
 438 $(\langle V_x \rangle / \sqrt{gd} = a^*(y/d)^2 + b^*(y/d))$ in solid lines. For all polynomial fits, $R^2 \geq 0.99$.

445 velocity profiles are not Bagnold-like, the inertial number is not constant with depth here,
 446 but decreases from the surface to the bottom (Fig. 7c).

454 4.2 Velocity Fluctuations

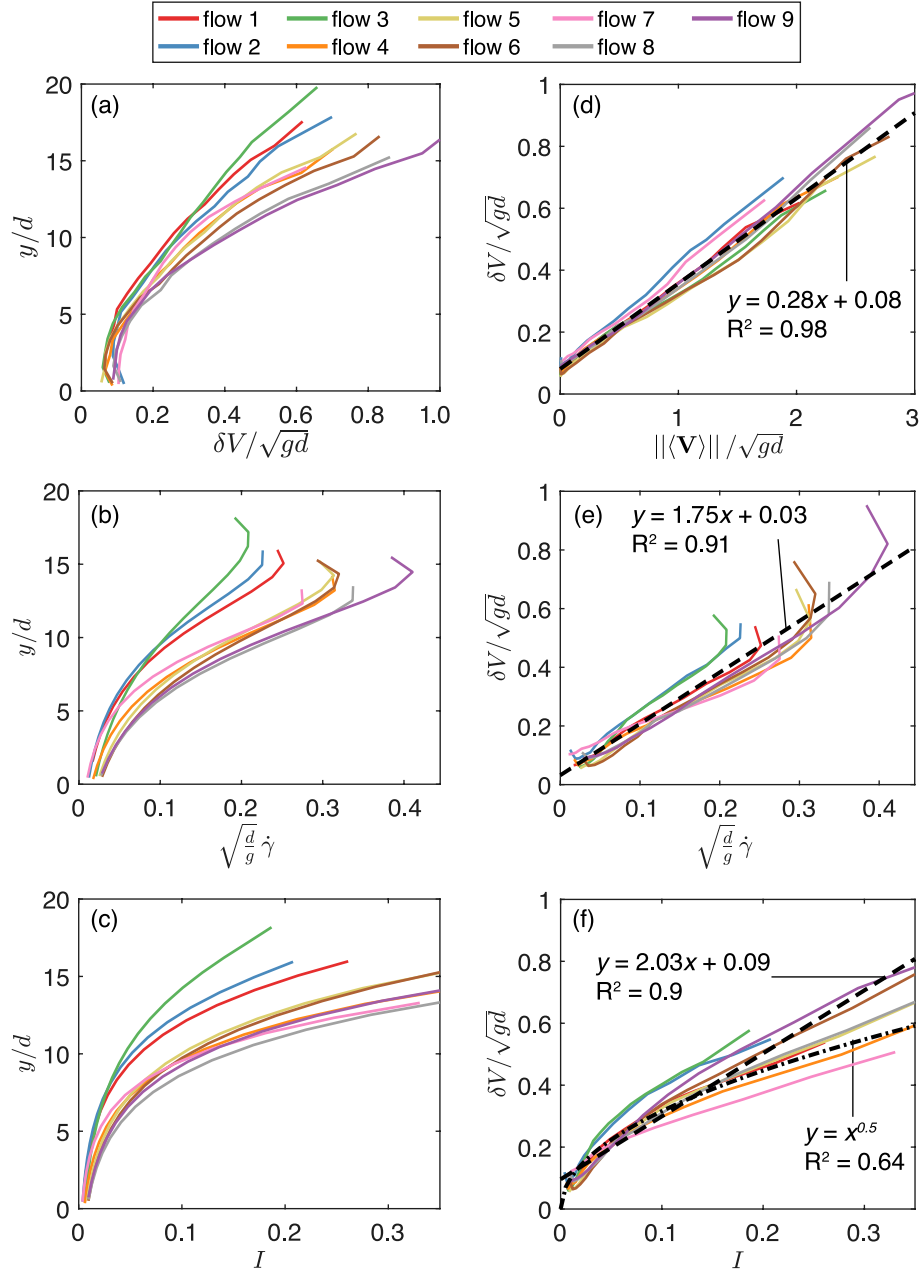
455 The high-frequency acoustic signal generated by granular flows is expected to arise
 456 mainly from particle collisions, , as indicated by Huang et al. [2007], though other ef-
 457 fects may play a role [Michlmayr et al., 2013]. Squeal noise associated with friction in
 458 granular media has been documented by Akay [2002] but, in the unconfined configura-
 459 tion of free surface granular flow, we hypothesize that normal forces between the cen-
 460 ters of colliding grains are larger than the sliding forces between surfaces of grains in con-
 461 tact, so we focus on the normal component of collisions. Such collisions occur when neigh-
 462 boring particles have different velocities, as a result of fluctuations about their mean ve-
 463 locities.

464 Velocity fluctuations, quantified by their mean squared values (the ‘granular tem-
 465 perature’) [Goldhirsch, 2008]

$$T = \delta V^2, \quad (5)$$

466 are known to be significant in granular flows. In general, however, granular temperature
 467 is not explicitly accounted for in the rheology of dense granular flows, except in the ex-
 468 tended kinetic theory [e.g. Berzi, 2014, Gollin et al., 2017]. Indeed, the relationship be-
 469 tween velocity fluctuations and the inertial number or other mean flow quantities has
 470 not yet been thoroughly investigated in dense granular flows. They are difficult to mea-
 471 sure experimentally, and even more so in the field [Berzi & Jenkins, 2011, Hill & Tan,
 472 2014]. The acoustic power, which is much easier to measure, may provide a unique tool
 473 to obtain quantitative measurements of granular temperature, as will be investigated be-
 474 low.

475 Fig. 7a shows that measured velocity fluctuations decrease from the surface to the
 476 bottom for all experiments and increase with slope angle. Using discrete element mod-
 477 eling, Hanes & Walton [2000] showed that the granular temperature profile is very dif-
 478 ferent at the side wall than it is within the core of the flow: the simulated granular tem-
 479 perature is, at the surface, the same at the side walls and across the flow, but increases
 480 with depth in the middle of the flow while decreasing with depth at the side walls, as
 481 observed in these experiments.



447 **Figure 7.** (a) Normalized fluctuating speed $\delta V/\sqrt{gd}$ (with $\sqrt{gd} \simeq 0.14$ m/s), (b) normalized
 448 shear rate $\sqrt{d/g}\dot{\gamma}$ (with $\sqrt{d/g} \simeq 0.014$ s) and (c) inertial number I , computed using the second
 449 order polynomials that provide the best fit to $\langle V_x \rangle$, as functions of flow depth y/d , for all of the
 450 experiments (colors). (d) to (f) Normalized fluctuating speed $\delta V/\sqrt{gd}$ as a function of (d) the
 451 mean flow speed $\|\langle \mathbf{V} \rangle\|/\sqrt{gd}$, (e) the normalized shear rate $\sqrt{d/g}\dot{\gamma}$ and (f) inertial number I . In
 452 panels (d) to (f), dashed lines show fits of the data with linear laws. In panel (f), the dash-dotted
 453 line shows a power-law (square root) fit of the data.

482 Even though velocity fluctuations about the mean look regular when averaged over
 483 volume and time, Figs. C1(a) and (b) in the Appendix and Movies 3 and 4 in the sup-
 484plementary material illustrate the existence of transient vortices of velocity fluctuations
 485 in our experiments, as observed by Kharel & Rognon [2017]. The size and intensity of
 486 these transient vortices seem to be related to the flow regime, leading to strong varia-
 487tion of velocity fluctuations (in space and time) where the flow is close to jamming, pos-
 488sibly contributing to acoustic emissions from these regions. The correlation length of these
 489velocity fluctuations is around 1 grain diameter in the y -direction and can reach up to
 490 $8d$ in the x -direction, decreasing with increasing slope (see Fig. C2 in Appendix C).

4.3 Relationship Between Mean Properties and Fluctuations

492 Granular temperature is expected to scale with the square of the shear strain rate,
 493 so that $\delta V \propto \dot{\gamma}$ [see e.g. Andreotti et al., 2013, Pouliquen, 2004]. Such a linear relation-
 494ship between δV and $\dot{\gamma}$ seems indeed to be satisfied (Fig. 7e), in very good agreement
 495with observations at the surface of granular flows by Pouliquen [2004] and in other con-
 496figurations [GDR MiDi, 2004]. If we try to fit the data by a power law, we get a power
 497equal to 2 with high R^2 . A higher R^2 is found when trying to relate the velocity fluc-
 498tuations to the mean downslope velocity $\langle V_x \rangle$ (Fig. 7d). The slightly higher R^2 may re-
 499sult from errors in the estimation of the gradient of the measured velocity profile. Any
 500power law relationship between velocity fluctuations and the inertial number is less clear,
 501with a smaller R^2 (Fig. 7f). This could, similarly, be due to the errors in the calcula-
 502tion of I . As a result, velocity fluctuations averaged in time and along one layer of grains
 503scale very well with shear rate and with mean velocity and to a lesser extent with the
 504inertial number:

$$\delta V \propto \langle V_x \rangle \propto \dot{\gamma} \propto I^{0.5}. \quad (6)$$

5 Signature of Flow Dynamics in the Acoustic Signal

506 Our objective is to quantitatively relate the characteristics of the seismic signal to
 507 those of the flow, in order to (i) get physical insights into the sources of acoustic emis-
 508sion and (ii) propose empirical scaling laws that can be used to recover flow properties
 509 from the recorded acoustic waves. As the range of configurations (slope angle, thickness)
 510 investigated here is not very large, it is hard to discriminate between power laws or lin-

ear trends. We will therefore systematically test these two types of empirical fits and quantify the associated R^2 .

5.1 Acoustic Frequencies

5.1.1 Orders of Magnitude of Possible Signal Frequencies

Let us first discuss the orders of magnitude of the signal frequencies that the physics of the granular flow could generate, based on our setup and on the observation of flow dynamics described in the previous sections. We have identified 6 physical processes that present different frequency signatures.

The frequency range of the signal is expected to be determined by the physics of a typical inter-particle collision, scaling with the inverse of the Hertzian contact time between two spheres of diameter d that have collided at relative velocity δV [Farin et al., 2015]. For impacts between such particles, Bachelet [2018] proposed the following expression for the amplitude-weighted mean signal frequency:

$$f_{Hertz} = a'_0 d^{-1} \delta V^{1/5}, \quad (7)$$

where

$$a'_0 \simeq 0.90 \left(\frac{E\sqrt{2}}{\pi\rho(1-\nu^2)} \right)^{2/5} \simeq 650 \text{ (m/s)}^{4/5}, \quad (8)$$

for $E = 74 \text{ GPa}$, $\rho = 2500 \text{ kg m}^{-3}$, and $\nu = 0.2$ the Young's modulus, density, and Poisson's ratio of the particles' glass. This implies that $140 \text{ kHz} < f_{Hertz} < 220 \text{ kHz}$ for $0.1 \times \sqrt{gd} < \delta V < \sqrt{gd}$, with $\sqrt{gd} = 0.14 \text{ m s}^{-1}$. While we won't discuss the validity of Bachelet [2018]'s theoretical prediction, and Farin et al. [2018] found the mean frequency of an impact on a rough bed to be between about 1/2 and 2/3 of the mean frequency of an impact on a smooth bed, this indicates that collisions between particles will generate signals at frequencies right up to the upper limit of our measurements.

In contrast, the coherent vertical oscillations of the particles, due to the motion of each layer over the one below (see section 3.1.3, Fig. 3), can be expected to cause signal modulation at frequencies f_{osc} that are about 1000 times smaller, with $33 \text{ Hz} < f_{osc} < 52 \text{ Hz}$. These oscillation frequencies are of the order of magnitude of $\delta V/d$, corresponding to a typical rate of collisions.

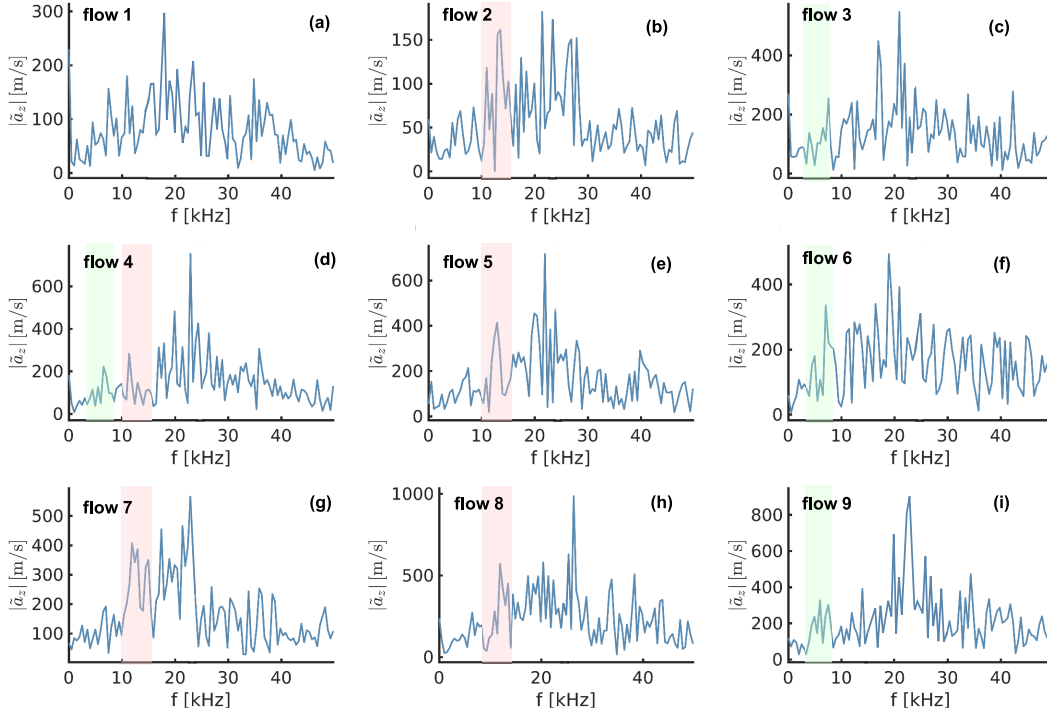
On the other hand, frequencies around $f_h \simeq 3 - 7 \text{ kHz}$ in the signal may originate from the typical period of the acoustic wave front propagation through the flow thick-

539 ness $h = 3$ cm, if we assume an acoustic wave velocity in granular flows of $100\text{-}200$ m s⁻¹
 540 (see e.g. Hostler [2004], Hostler & Brennen [2005], Mouraille & Luding [2008]). Note that
 541 the velocity of acoustic signals in granular material varies strongly depending on the con-
 542 fining pressure, packing fraction, material involved, etc. Liu & Nagel [1993] found val-
 543 ues varying from about 60 to 280 m s⁻¹ depending upon the kind of velocity measured,
 544 van den Wildenberg et al. [2013] between 80 m s⁻¹ and 150 m s⁻¹ and Bonneau et al.
 545 [2008] between 40 m s⁻¹ and 80 m s⁻¹.

546 Observations show that the flow thickness oscillates slightly with time (see Fig. A1
 547 in the Appendix), possibly due to compression/dilatation waves in the media or to the
 548 complex heterogeneity of the flow (see section 4.2 and Fig. C1 in the Appendix). The
 549 typical period of these oscillations is 1 s, possibly generating signals at frequencies $f_{flow} \simeq$
 550 1 Hz.

551 Movies of velocity fluctuations (Movies 3 and 4 in the supplementary material) demon-
 552 strate the appearance and disappearance of vortices of velocity fluctuations (cf Fig. C1
 553 in the Appendix). These vortices may be similar to the turbulent vortices that develop
 554 in rivers and apply fluctuating forces on the bed roughness, generating seismic signals
 555 over a wide frequency range $1\text{-}10^5$ Hz [Gimbert et al., 2014]. Turbulent vortices form close
 556 to the flowing-static interface due to the shear stress applied by the flow on the bed. The
 557 vortices, once formed, grow through coalescence until they reach the thickness of the flow,
 558 then break up into smaller vortices, transferring flow energy towards smaller scales [Kol-
 559 mogorov, 1941]. The highest frequencies generated by the vortices are related to the min-
 560 imum vortex size, i.e. the Kolmogorov microscale, which may not be reachable in a gran-
 561 ular flow in which the minimum vortex scale is in theory at least two particle diameters
 562 $2d$. Therefore, in granular flows, we expect lower frequencies to be generated by vortices
 563 than those that can be observed in a liquid flow. The typical size of the observed vor-
 564 tices in our granular flows is about $5\text{-}8d \simeq 1 - 1.6$ cm and they travel within the flow
 565 at velocities of around 1 m s⁻¹. Therefore, these granular vortices may generate waves
 566 at frequencies $f_v \simeq 60 - 100$ Hz.

567 Finally, if we assume a wave velocity in the plate of $v_g \simeq 1000$ m s⁻¹, the reso-
 568 nance of the $L \times l = 10$ cm \times 6.5 cm acoustically isolated plate gives rise to fundamen-
 569 tal resonance frequencies $f_{p1} \simeq v_g/l \simeq 15$ kHz and $f_{p2} \simeq v_g/L \simeq 10$ kHz, with
 570 higher resonances possible throughout the measured frequency range. Let us now an-



574 **Figure 8.** High-frequency ($f > 1$ kHz) spectral amplitude measured for all flows. Letters (a)
 575 to (i) refer to flow numbers 1 to 9, corresponding to angles (a-c) $\theta = 16.5^\circ$, (d-f) $\theta = 17.2^\circ$ and
 576 (g-i) $\theta = 18.1^\circ$ and to increasing flow thickness along each row (see Table 1 for details). Light
 577 pink areas correspond to the frequency range associated with fundamental plate resonances, be-
 578 tween f_{p1} and f_{p2} , and light green areas to the frequency range f_h associated with waves trapped
 579 in the granular layer.

571 analyze the frequency content of the measured signal and compare it to these expected fre-
 572 quencies.

573 *5.1.2 Comparison with Measured Frequencies*

580 Fig. 8 shows that signals are generated throughout the frequency range we are able
 581 to measure, consistent with our expectations of inter-particle collisions. Even though no
 582 clear peaks appear in the high-frequency spectra, there are indications of peaks at fre-
 583 quencies $3 \text{ kHz} < f < 10 \text{ kHz}$ for almost all the flows, which may correspond to waves
 584 trapped within the flowing granular layer (with expected frequency range $3 \text{ kHz} < f_h <$
 585 10 kHz). These are highlighted in light green in Fig. 8(c), (d), (f), and (i). Other peaks
 586 appear at frequencies between 10 and 20 kHz, which may be related to the plate's fun-

587 fundamental resonances (at $f_{p1} \simeq 10$ kHz and $f_{p2} \simeq 15$ kHz), as illustrated in light pink
 588 in Fig. 8(b), (d), (e), (g), and (h).

589 In the low-frequency range, Fig. 9 shows clear peaks in signal envelope amplitude
 590 between 28 Hz and 50 Hz. These frequencies f_{mod} of the acoustic amplitude modulation
 591 are clearly in the range of the frequencies f_{osc} associated with the vertical oscillation of
 592 the particles at the surface of the flow (Fig. 10c). Indeed, accounting for error, all mod-
 593 ulation frequencies f_{mod} are within the 30 to 60 Hz frequency range of f_{osc} , as highlighted
 594 in light gray in Figs. 9(a) and 9(i).

595 The acoustic amplitude modulation frequency increases as a function of the iner-
 596 tial number: f_{mod} is extracted from a Gaussian fit in the range 10-70 Hz of the spectrum
 597 (Fig. 9), and shown as a function of $\langle I \rangle$ in Fig. 10b. In addition, almost all the flows ex-
 598 hibit an increase of spectral amplitude at frequencies between 1 Hz to 3 Hz (see light pink
 599 region in Fig. 9). This may correspond to the frequencies of flow oscillations $f_{flow} \simeq$
 600 1 Hz. Some peaks at 15 to 25 Hz also appear for some flows. Some flows also show a small
 601 increase of spectral amplitude at around 60-70 Hz (see Fig. 9(c) and (f) where this fre-
 602 quency range is highlighted in light green) that could be compatible with frequencies $f_v \simeq$
 603 60 – 100 Hz associated with vortices of the velocity fluctuations.

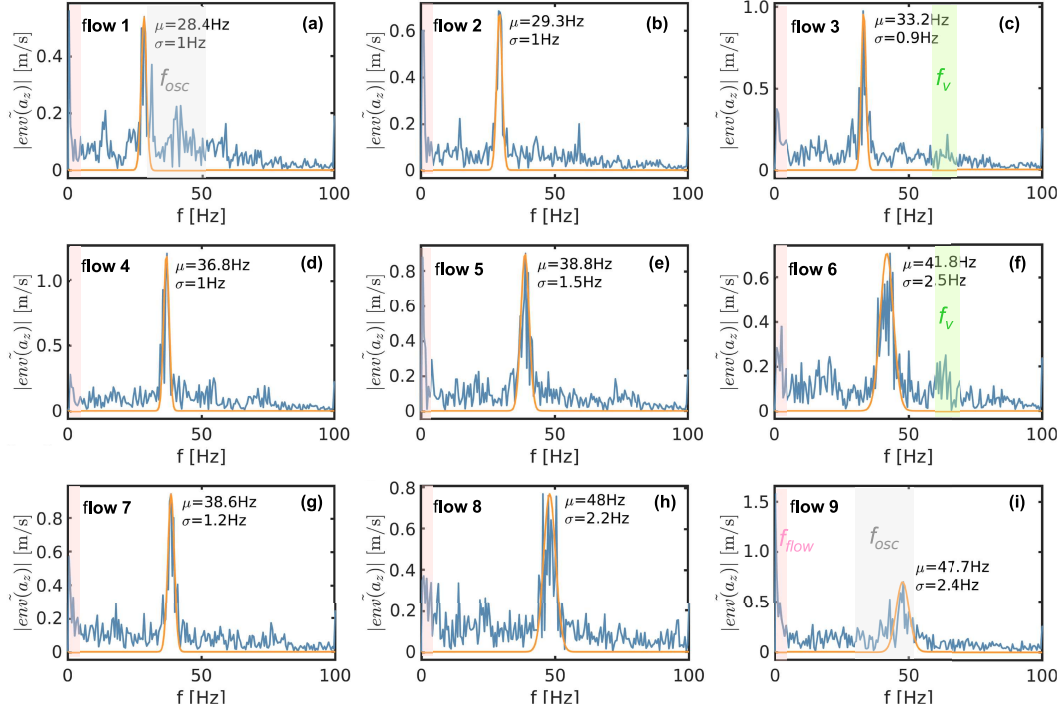
614 5.2 Acoustic Power

615 5.2.1 Power Laws and Comparison with Field Observations

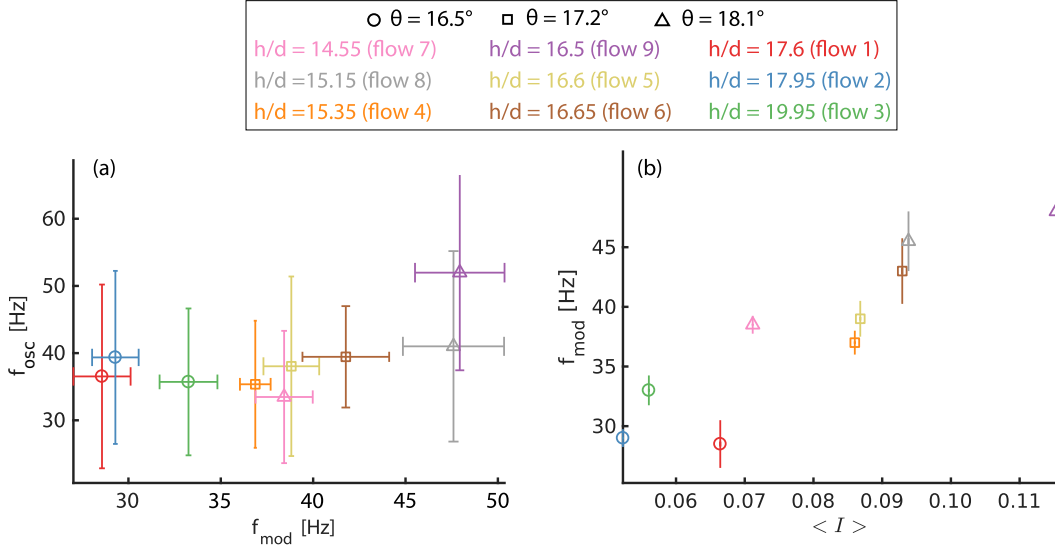
616 We investigate here the relationship between the acoustic power and the proper-
 617 ties of the flow, averaged over the granular depth. Figs. 11(a) and (b) show that the acous-
 618 tic power increases with the depth-averaged velocity fluctuations $\langle \delta V \rangle$ and inertial num-
 619 ber $\langle I \rangle$. The range of parameter variation is too low to determine a functional relation-
 620 ship but, conducting a linear regression in log-space, our data are compatible with power
 621 law relationships

$$\Pi_{el} \propto \langle \delta V \rangle^{3.1 \pm 0.9} \propto \langle I \rangle^{2.2 \pm 0.4}. \quad (9)$$

630 In the field, the seismic power can be calculated from the signal measured at seis-
 631 mic stations and then related to the mean flow velocity, deduced by inverting low-frequency
 632 seismic data [Allstadt, 2013, Hibert et al., 2017b]. Field experiments, in which single blocks
 633 of different masses were released down a gully, have also shown a correlation between the

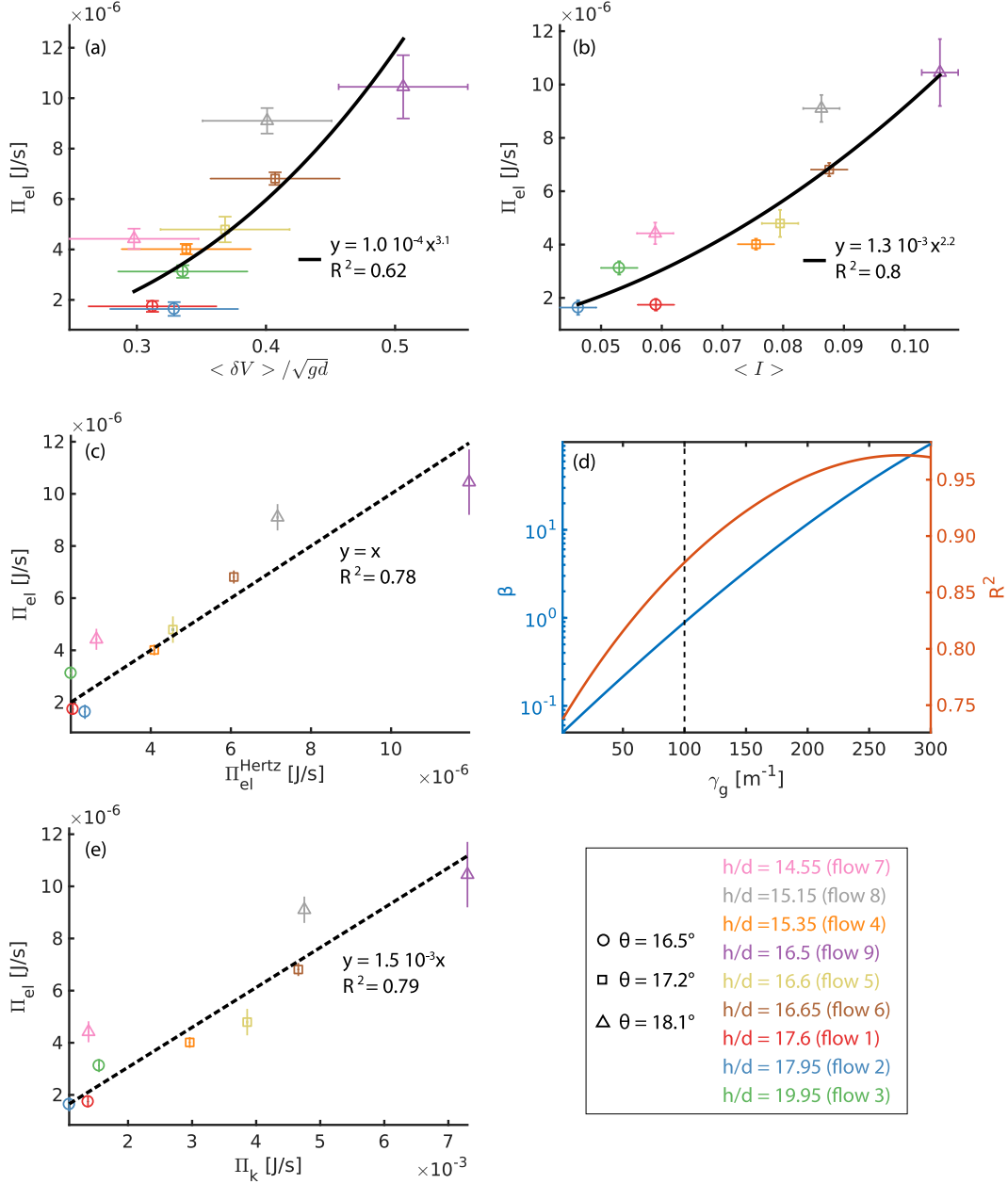


604 **Figure 9.** Low-frequency ($f < 100$ Hz) spectral amplitude measured for all flows. Letters
 605 (a) to (i) refer to flow numbers 1 to 9, corresponding to angles (a-c) $\theta = 16.5^\circ$, (d-f) $\theta = 17.2^\circ$
 606 and (g-i) $\theta = 18.1^\circ$ and to increasing flow thickness along each row (see Table 1 for details). The
 607 orange curves correspond to the Gaussian fits (see Fig. 5e). Light gray areas in Fig. (a) and (i)
 608 correspond to the frequency range associated with particle oscillations f_{osc} , light pink zones on
 609 all the figures correspond to the frequency range of flow oscillations f_{flow} and light green zones
 610 to frequency range of vortices f_v .

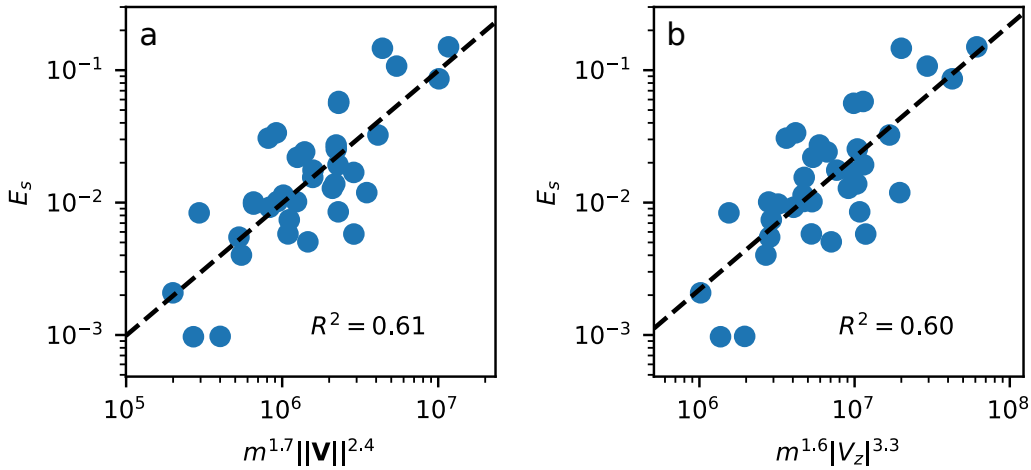


611 **Figure 10.** (a) Particles' vertical oscillation frequency f_{osc} , as a function of the frequency
 612 f_{mod} of the acoustic amplitude modulation. (b) Acoustic modulation frequency f_{mod} as a func-
 613 tion of the average inertial number $\langle I \rangle$.

634 velocity \mathbf{V} of a block before impact and the seismic energy E_s released during impact
 635 [Hibert et al., 2017c]. With this dataset, we conducted a linear regression of $\log E_s$ against
 636 $\log m$ and either $\log \|\mathbf{V}\|$ or $\log |V_z|$, where m is the mass of a block and \mathbf{V} its velocity
 637 before impact, with vertical component V_z . When considering the modulus of the ve-
 638 locity, we found that the seismic energy scales as $E_s \propto \|\mathbf{V}\|^{2.4 \pm 0.5}$ (Figure 12a). When
 639 considering only the modulus of vertical component of the velocity before impact V_z , the
 640 seismic energy scales as $E_s \propto |V_z|^{3.3 \pm 0.8}$ (Figure 12b). Note that the precision on these
 641 best-fit exponents is low, since the fit quality of this form is moderate, with R^2 between
 642 0.6 and 0.7, and that they were obtained for single blocks and not for granular flows. Nev-
 643 ertheless, the dependence of E_s on impact velocity may be compared to the dependence
 644 of Π_{el} on $\langle \delta V \rangle$ in our laboratory measurements, in Eq. (9). Note that similar scaling laws
 645 linking seismic wave characteristics to dynamic properties have been found for granu-
 646 lar flows and for natural single-block rockfalls (e.g. [Hibert et al., 2017b, 2017c, Schnei-
 647 der et al., 2010]).



622 **Figure 11.** Radiated elastic power Π_{el} as a function of (a) normalized average velocity fluctu-
 623 ations $\langle \delta V \rangle / \sqrt{gd}$ (with $\sqrt{gd} \simeq 0.14$ m/s) and (b) average inertial number $\langle I \rangle$. (c) Experimental
 624 Π_{el} versus analytical elastic power Π_{el}^{Hertz} for granular attenuation $\gamma_g = 100$ m $^{-1}$. (d) Slope β of
 625 the best single-regressor linear fit between values $\Pi_{el}^{Hertz}(\gamma_g)$ and Π_{el} , and the associated sum of
 626 squared residuals R^2 , as a function of the attenuation coefficient γ_g . The vertical black dashed
 627 line highlights the case of $\gamma_g = 100$ m $^{-1}$, the value for which the model gives about the same
 628 result as the measurements, i.e. $\Pi_{el}^{Hertz} / \Pi_{el} \simeq 1$. (e) Comparison between the measured radiated
 629 elastic power Π_{el} and available kinetic power Π_k .



648 **Figure 12.** a) Energy E_s of the seismic signal generated at each individual block impact, as
 649 a function of $m^\alpha ||\mathbf{V}||^\beta$, for block mass m and modulus of the velocity before impact $||\mathbf{V}||$, with
 650 the exponents α and β inferred to get the best fit by linear regression; b) As a), except with $|V_z|$
 651 rather than $||\mathbf{V}||$. All quantities are in SI units and rockfall data are from Hibert et al. [2017c].

652 **5.2.2 Simple Model for Acoustic Emission**

653 Based on the understanding of the seismic source gained above, we propose a sim-
 654 ple model that makes it possible to recover the radiated elastic power from particles' ve-
 655 locity fluctuations (i.e. the square root of the granular temperature). We assume that
 656 (i) the elastic waves are generated during binary collisions between particles in adjacent
 657 layers, at speeds corresponding to the particles' fluctuation velocities, (ii) collisions are
 658 described by the Hertz contact law and the radiated elastic energy is the work done by
 659 the impact force during the contact [Farin et al., 2015, Johnson, 1987], and (iii) the acous-
 660 tic waves propagate from the layer where they are generated down to the bottom of the
 661 channel. Attenuation in granular media is frequency dependent [Leclercq et al., 2017,
 662 Legland et al., 2012, Martin et al., 2018], and evolves with the reconfiguration of force
 663 chains during the flow (as illustrated by Lherminier et al. [2014]), but for the sake of sim-
 664 plicity we assume here that attenuation with distance to the bottom is frequency inde-
 665 pendent, with constant attenuation coefficient γ_g .

666 Attenuation in granular media varies strongly, depending on the confining pressure,
 667 packing fraction, signal frequency, etc. Different values are reported in the literature, vary-

668 ing between 15 m^{-1} and 150 m^{-1} : e.g. Voronina & Horoshenkov [2004] and Chrzaszcz
 669 [2016] found $\gamma_g = 100 \text{ m}^{-1}$ and Hostler & Brennen [2005] found values between 25 m^{-1}
 670 and 50 m^{-1} .

671 In our model, the total elastic power is obtained by summing up the contributions
 672 of all layers:

$$\Pi_{el}^{Hertz} = \sum_{i=1}^n N_i W_{el,Hertz}^i e^{-\gamma_g y_i}, \quad (10)$$

673 where $W_{el,Hertz}^i$ is the typical elastic energy radiated during the impact of a particle in
 674 layer i , y_i is the height of the center of the layer i , $e^{-\gamma_g y_i}$ is the exponential decay of the
 675 wave energy with distance to the bottom, N_i is the rate of impacts in layer i and n is
 676 the number of layers.

677 The elastic energy radiated during an impact is computed from Hertz contact the-
 678 ory [Farin et al., 2015], under the assumption that the force between two particles is trans-
 679 mitted, attenuated but undistorted, to a thin plate with a frequency-independent veloc-
 680 ity response to forcing. Then,

$$W_{el,Hertz}^i = a_0 \left(\frac{d}{2} \right)^5 (\delta V(y_i))^{11/5}, \quad (11)$$

681 with $\delta V(y_i)$ the velocity fluctuation in layer i and a_0 a prefactor involving the elastic pa-
 682 rameters of the particles and the PMMA plate [Bachelet et al., 2018]. For bending mod-
 683 ulus, density, and thickness of the plate $B = 425 \text{ kg m}^2 \text{ s}^{-2}$, $\rho_p = 1180 \text{ kg m}^{-3}$, and
 684 $h_p = 0.01 \text{ m}$, and Young's modulus, Poisson's ratio, and density of the glass particles
 685 $E = 74 \text{ GPa}$, $\nu = 0.4$, and $\rho = 2500 \text{ kg m}^{-3}$,

$$a_0 \simeq 2.1 \frac{1}{\sqrt{B\rho_p h_p}} \left(\frac{E}{2(1-\nu^2)} \rho^4 \right)^{2/5} \simeq 1.4 \times 10^8 \text{ kg m}^{-5} (\text{m s}^{-1})^{-1/5}. \quad (12)$$

686 The rate of impacts in layer i is given by:

$$N_i = \frac{\phi l L}{\pi \left(\frac{d}{2} \right)^2} f_i, \quad (13)$$

687 with the ratio of areas corresponding to the number of particles above the monitored plate
 688 of size $L \times l$, and f_i equal to the number of impacts per particle and per unit time. Im-
 689 pacts are assumed to occur when a particle overrides another particle of the layer be-
 690 low at their relative downslope velocity so that

$$f_i = \frac{\langle V_x \rangle(y_i) - \langle V_x \rangle(y_{i-1})}{d} = \dot{\gamma}(y_i). \quad (14)$$

691 Combining expressions (10), (11), (13) and (14) leads to the final expression of the an-
 692 alytical radiated elastic power

$$\Pi_{el}^{Hertz} = \frac{a_0 \phi l L}{8\pi} d^3 \sum_i \dot{\gamma}(y_i) \delta V(y_i)^{11/5} e^{-\gamma_g y_i}. \quad (15)$$

693 Using Eq. (15), the acoustic power is expected to scale as

$$\Pi_{el} \propto \langle \delta V \rangle^{16/5}. \quad (16)$$

694 Because our optical observations showed that $\delta V \propto (\dot{\gamma}d) \propto I^{0.5}$, Π_{el} is also predicted
 695 to be proportional to $\langle \dot{\gamma} \rangle^{3.2}$ or $\langle I \rangle^{1.6}$. Despite our inability to measure all power imparted
 696 to the plate, due to the limited frequency range of our accelerometers, this is in very good
 697 agreement with the scaling observed in Fig. 11a, which suggests $\Pi_{el} \propto \langle \delta V \rangle^{3.1 \pm 0.9}$, and
 698 in reasonable agreement with the scaling observed in Fig. 11b, which suggests $\Pi_{el} \propto$
 699 $\langle I \rangle^{2.2 \pm 0.4}$. Nonetheless, as previously noted, the narrow range of our experiments makes
 700 it very difficult to discriminate between different power-law exponents or functional re-
 701 lationships.

702 To compare our observations with those of Taylor & Brodsky [2017], we have to
 703 note that the value E_a that they called ‘acoustic energy’ is a term proportional to the
 704 square of the acceleration, rather than the square of velocity. As a consequence of this
 705 and of Eq. (7), which indicates that typical signal accelerations are a factor $a'_0 d^{-1} \delta V^{1/5}$
 706 larger than typical signal velocities, we expect that $E_a \propto \langle \delta V \rangle^{2/5} \Pi_{el}$. This would im-
 707 ply that, according to our theory, $E_a \propto \langle \delta V \rangle^{18/5} = \langle \delta V \rangle^{3.6}$ or, if we assume the power
 708 laws $\delta V \propto I^{0.5}$ and $\Pi_{el} \propto \langle I \rangle^{2.2 \pm 0.4}$ of equations (6) and (9), that $E_a \propto \langle I \rangle^{2.4 \pm 0.4}$.
 709 Taylor & Brodsky [2017]’s observations, however, suggest that $E_a \propto I$. This difference
 710 may be due to the fact that their setting is very different from ours, to error in their cal-
 711 culation of I (which they estimate by assuming a shear layer thickness of $5d$, for all ex-
 712 periments) or to the limitations of our simple model.

713 The key parameter in the calculation of Π_{el}^{Hertz} is the attenuation factor. If we take
 714 $\gamma_g = 100 \text{ m}^{-1}$, we obtain a very good agreement with the measured acoustic power (Fig.
 715 11c). However, the value of Π_{el}^{Hertz} is very sensitive to γ_g , as shown in Fig. 11d. For ex-
 716 ample, if $\gamma_g = 50 \text{ m}^{-1}$, $\Pi_{el}^{Hertz} \simeq 0.5 \Pi_{el}$. Figs. 13(a) and (b) show that, with $\gamma_g =$
 717 100 m^{-1} , the main contributions to the acoustic power come from the grains near the
 718 surface, while with $\gamma_g = 300 \text{ m}^{-1}$, they come from the grains located in the middle of
 719 the granular layer, where velocities and velocity fluctuations are small. Bachelet et al.

[2018]’s measurements of acoustic energy transmission through static grain packs suggest an attenuation constant $\gamma_g = 220 \text{ m}^{-1}$ for our $d = 2 \text{ mm}$ grains, but such transmission is affected by the structure of the grain pack [Lherminier et al., 2014], which may be significantly different in granular flows. Precise attenuation measurements will be a crucial step to further validate our simple model and will be performed in the future.

Another key issue is the difference between the fluctuations measured near the side walls and those within the flow, as observed in the discrete element simulations of Hanes & Walton [2000] and discussed in section 4.2. To assess how the predicted acoustic power would change if measurements were performed in the flow’s center, we calculate Π_{el}^{Hertz} for profiles of the fluctuating velocity that mimic those in the simulations of Hanes & Walton [2000] (their Fig. 15). Specifically, we take the same value δV_s of the fluctuating velocity δV as at the free surface but suppose that δV , instead of decreasing down to the bottom, increases linearly to reach $\delta V(d) = 1.2\delta V_s$. This assumption corresponds to

$$\Pi_{el}^{Hertz} = \sum_i \frac{\phi l L}{\pi(d/2)^2} f_i a_0 (d/2)^5 (1.2\delta V_s(1 - y_i/h) + \delta V_s y_i/h)^{11/5} e^{-\gamma_g y_i}. \quad (17)$$

Assuming that the collision frequency is $f_i = \delta V_i/d = (1.2\delta V_s(1 - y_i/h) + \delta V_s y_i/h)/d$ further leads to

$$\Pi_{el}^{Hertz} = \frac{a_0 \phi l L h d}{8\pi} \delta V_s^{16/5} \int_0^1 (1.2 - 0.2z)^{16/5} e^{-\gamma_g h z} dz. \quad (18)$$

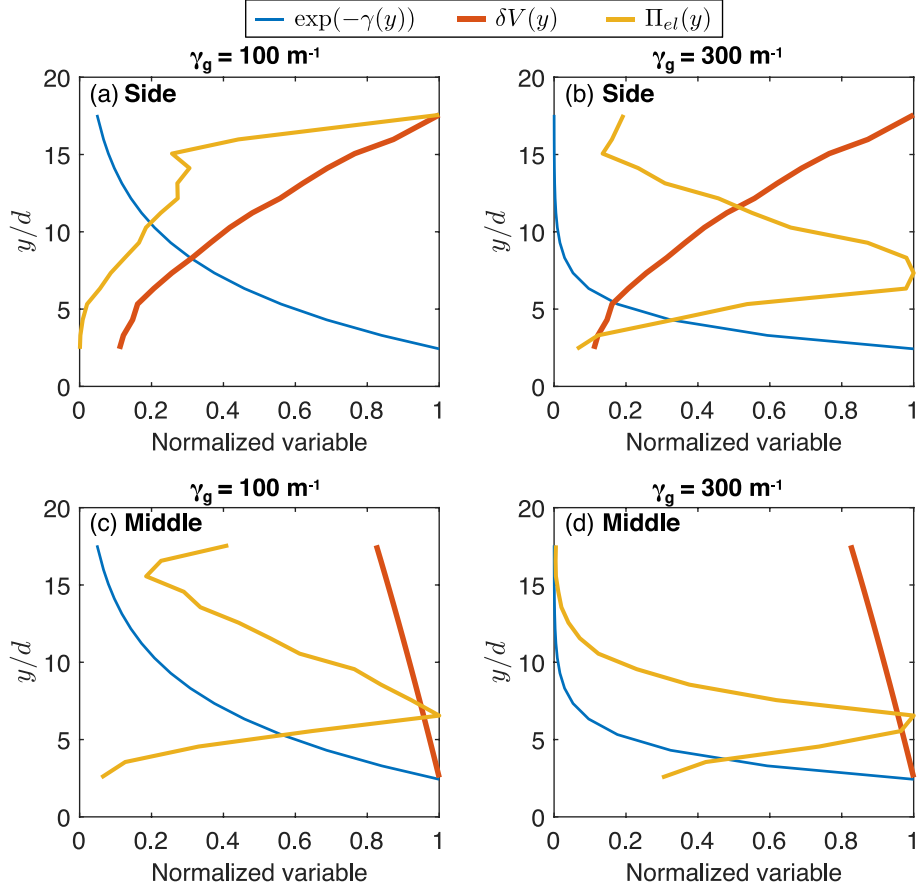
Note that when we make this assumption on the $\delta V(y)$ profile, the main contribution to the acoustic power comes from slightly below the middle of the granular layer, regardless of whether the attenuation coefficient is $\gamma_g = 100 \text{ m}^{-1}$ or $\gamma_g = 300 \text{ m}^{-1}$ (Figs. 13(c) and (d)).

5.2.3 Acoustic versus Kinetic Energy

Finally, we construct a model linking acoustic emissions to the mean kinetic energies of grains in each flow layer,

$$E_k^i = \frac{\pi \rho d^3}{12} (\|\langle \mathbf{V} \rangle\| (y_i)^2 + \delta V (y_i)^2), \quad (19)$$

by adding to our previous model the somewhat arbitrary assumption that the conversion coefficient from kinetic to attenuation-adjusted acoustic energy, i.e. the energy ratio or acoustic efficiency $W_{el,Hertz}^i/E_k^i$, is constant for each impact and equal to ξ . We then replace the term $W_{el,Hertz}^i$ in expression (10) by ξE_k^i to recover the prediction $\Pi_{el} =$



740 **Figure 13.** (a),(b) Normalized contributions $N_i W_{el,Hertz}^i e^{-\gamma_g y_i}$ to analytical acoustic
 741 power Π_{el} , as a function of depth y_i/d and computed using the fluctuating speed δV mea-
 742 sured along the side of the flow in experiment 1, for (a) $\gamma_g = 100 \text{ m}^{-1}$ and (b) $\gamma_g = 300 \text{ m}^{-1}$.
 743 (c),(d) Equivalent normalized contributions, assuming a linear granular temperature profile in-
 744 creasing with depth, as might be observed in the middle of the flow, for (c) $\gamma_g = 100 \text{ m}^{-1}$ and (d)
 745 $\gamma_g = 300 \text{ m}^{-1}$. In each panel, attenuation $\exp(-\gamma_g y)$ is also represented.

753 $\xi\Pi_k$, for available kinetic power

$$\Pi_k = \sum_i N_i E_k^i e^{-\gamma_g y_i}. \quad (20)$$

754 Fig. 11e shows that, over our experiments, the measured acoustic power is approximately
755 proportional to Π_k and the implied energy ratio is $\xi = 1.5 \times 10^{-3}$.

756 In contrast, the experiments of Bachelet et al. [2018] measured a mean energy con-
757 version coefficient, after adjustment for attenuation, of $\xi \simeq 0.13$. Basal properties in
758 those experiments were identical to this study's, but grains had greater mean density ρ ,
759 Young's modulus E , diameter d , and velocity \mathbf{V} . Furthermore, each impact was between
760 a falling grain and a static, horizontal base, so that, generalising δV to be the normal
761 impact velocity, $\delta V \simeq \|\mathbf{V}\|$. In our case, meanwhile, $\Pi_{el}^{Hertz} \simeq \Pi_{el}$ and Π_k are domi-
762 nated by contributions from near-surface impacts, for which Figure 7d indicates that $\delta V \simeq$
763 $0.28\|\mathbf{V}\|$. Since, generalising the definitions of $W_{el,Hertz}^i$, E_k^i , $\|\langle \mathbf{V}^2 \rangle\|$ and Hertz prefac-
764 tor $a_0 \propto (E\rho^4)^{2/5}$ to apply to both cases,

$$W_{el,Hertz}^i/E_k^i = \frac{3a_0 d^2}{8\pi\rho} \frac{\delta V^2}{\|\langle \mathbf{V}^2 \rangle\|} \delta V^{1/5}, \quad (21)$$

765 these differences explain Bachelet et al. [2018]'s measurement of a much larger ξ . Equa-
766 tion (21) also suggests that Π_{el}/Pi_k is approximately constant over our experiments only
767 because $\Pi_{el} \simeq \Pi_{el}^{Hertz}$, the base and grains are kept constant, and the nature of our flows
768 does not vary significantly.

769 However, the energy ratio of 1.5×10^{-3} is comparable to that observed in the field
770 for rockfalls, despite acoustic energy emission depending strongly on the highly variable
771 bed response. As an example, values of $\xi \simeq 10^{-5} - 10^{-3}$ were found for rockfalls on
772 La Réunion Island [Hibert et al., 2011], on Montserrat Island [Levy et al., 2015] and in
773 the French Alps [Deparis et al., 2008].

774 6 Conclusion

775 As seismic waves generated by landslides are continuously recorded by seismic net-
776 works, detailed analysis of these signals provides a new way to collect data on the dy-
777 namics and rheology of natural flows. This is, however, only possible if quantitative re-
778 lationships between the flow properties and the acoustic signal characteristics are estab-
779 lished.

780 In the experiments reported here, we provide new quantitative insights into the ori-
781 gin of the acoustic signals generated by dense, almost steady and uniform granular flows
782 in which persistent contact networks link nearly static basal grains to energetic grains
783 near the surface. By capturing and analyzing high-speed camera footage, we measured
784 the base-normal profiles of mean flow velocity and of root mean square velocity fluctu-
785 ations, at the flows' lateral boundary, and demonstrated relationships between the fluctu-
786 ations, the mean velocity, the local shear rate and the local inertial number. Mean-
787 while, by capturing and processing accelerometer data, we could associate the flows' acous-
788 tic signals with observed flow properties and other physical phenomena: inter-particle
789 collisions, fundamental resonances of the flow's base, acoustic standing waves within the
790 flow, vortices of velocity fluctuations, coherent shear and macroscopic flow variations.
791 Then, using the approach of Farin et al. [2016], we estimated the rate of acoustic energy
792 transmission from each flow to its base and empirically related this power to our mea-
793 surements of both the depth-averaged root mean square velocity fluctuations within the
794 flow and the depth-averaged inertial number, finding the former relation to be consis-
795 tent with an analytical model in which internal shear leads to Hertzian collisions through-
796 out the flow, the normal forces of which are transmitted, attenuated but undistorted, to
797 a thin elastic plate.

798 More precisely, our results are consistent with a rate of seismic energy emission,
799 from each region of a granular flow, proportional to the 8/5th power of its granular tem-
800 perature (the mean squared value of velocity fluctuations). Beyond the interpretation
801 of the generated acoustic signal in terms of granular flow properties, this suggests a method
802 for measuring velocity fluctuations within granular flows, which may help improve our
803 understanding of the behavior of natural flows near boundaries. Indeed, Artoni & Richard
804 [2015b] suggested that velocity fluctuations i) are a key ingredient to be included in mod-
805 els describing dense granular flows in the vicinity of an interface and ii) appear in scal-
806 ing laws reproducing the effective friction at lateral walls. More specifically, force fluctu-
807 ations related to velocity fluctuations may trigger slip events even if the system is glob-
808 ally below the slip threshold [Artoni & Richard, 2015b]. Furthermore, granular temper-
809 ature is a key parameter of kinetic theories. Its measurement in dense granular flows will
810 help constrain attempts to extend this theory to dense granular flows [Berzi, 2014].

811 Finally, we consider a distinct acoustic signal, identified at frequencies around a
812 thousand times lower than the maximum measured signal frequency. This signal is shown

813 to correspond to the displacement of particles over one another, related to the coherent
814 relative motion of the grain layers. This seems to result from the quasi monodispersity
815 of the particles involved in these experiments and can be compared to signals identified
816 in the investigation of “booming dunes”.

817 Further studies should investigate the effects of particle size and shape on the gen-
818 erated acoustic signals and extend the range of bed slopes (i.e. velocities), so as to be
819 able both to better discriminate scaling laws between the characteristics of the flow and
820 those of the acoustic signal, and to examine the range of validity of such scaling laws.

821 **Notation**

- 822 \mathbf{a}'_0 Hertzian frequency coefficient ($(\text{m/s})^{4/5}$) (see Eq. 8)
- 823 \mathbf{a}_0 Hertzian energy coefficient ($\text{kg m}^{-5} (\text{m/s})^{-1/5}$) (see Eq. 12)
- 824 \mathbf{a}_z Vibratory acceleration of the basal plate (m s^{-2})
- 825 $|\tilde{\mathbf{a}}_z|$ Amplitude spectrum of the vibratory acceleration (m s^{-1})
- 826 $\mathbf{a}^*, \mathbf{b}^*$ Coefficients of a best-fit polynomial for a mean downslope velocity profile (–)
- 827 \mathbf{B} Bending stiffness of the basal plate (J)
- 828 \mathbf{d} Representative grain diameter (m)
- 829 \mathbf{E} Young’s modulus of the grains’ material (Pa)
- 830 \mathbf{E}_a ‘Acoustic energy’ defined by Taylor & Brodsky [2017] ($\text{m}^2 \text{s}^{-2}$)
- 831 \mathbf{E}_k^i Mean kinetic energy of a grain in layer i (J)
- 832 \mathbf{E}_s Seismic energy generated by a block impact of Hibert et al. [2017c] (J)
- 833 \mathbf{f} Frequency of the vibration signal (Hz)
- 834 \mathbf{f}_i Theoretical number of impacts per particle in layer i , per time unit (s^{-1})
- 835 $\mathbf{f}_{\text{Hertz}}$ Mean signal frequency predicted by Bachelet [2018] (Hz) (see Eq. (7))
- 836 $\mathbf{f}_h, \mathbf{f}_{p1}, \mathbf{f}_{p2}$ Frequencies associated with trapped waves and fundamental resonances
837 of the basal plate (Hz) (see section 5.1.1)
- 838 $\mathbf{f}_{\text{flow}}, \mathbf{f}_v$ Frequencies associated with macroscopic flow variation and vortices of veloc-
839 ity fluctuations (Hz) (see section 5.1.1)
- 840 \mathbf{f}_{osc} Frequency of grain oscillation during coherent shear (Hz)
- 841 \mathbf{f}_{mod} Frequency of acoustic modulation (Hz)
- 842 \mathbf{g} Gravitational acceleration (m s^{-2})
- 843 \mathbf{h} Flow thickness (m)
- 844 \mathbf{h}_g Gate elevation (m)
- 845 \mathbf{h}_p Thickness of the basal plate (m)
- 846 $\mathbf{I}, \langle \mathbf{I} \rangle$ Local and depth-averaged inertial number (–) (see Eq. (4))
- 847 \mathbf{L}, \mathbf{l} Length and width of the acoustically isolated plate (m)
- 848 \mathbf{M} Mass of the acoustically isolated plate (g)
- 849 \mathbf{N}_i Number of impacts per unit time in particle layer i (s^{-1})
- 850 \mathbf{n} Number of particle layers (–)
- 851 \mathbf{P} Hydrostatic pressure (Pa)
- 852 \mathbf{T} Granular temperature ($\text{m}^2 \text{s}^{-2}$)

853	t	Time (s)
854	$\mathbf{V} = (\mathbf{V}_x, \mathbf{V}_y)$	Grain velocity, downslope and normal to the base (m s^{-1})
855	$\langle \mathbf{V} \rangle = (\langle \mathbf{V}_x \rangle, \langle \mathbf{V}_y \rangle)$	Average velocities within each layer (m s^{-1})
856	$\mathbf{V}_{xs}, \langle \langle \mathbf{V}_x \rangle \rangle$	Surficial and depth-averaged mean downslope grain velocity (m s^{-1})
857	v_g	Group velocity of the A_0 mode in PMMA ($\simeq 1000 \text{ m s}^{-1}$)
858	v_z	Normal vibration velocity of the plate (m s^{-1})
859	w	Thickness of the layers over which averages are calculated (m)
860	W_{el}	Radiated elastic energy (J)
861	$W_{el,Hertz}^i$	Theoretical energy radiated from a collision in layer i (J)
862	x, y	Downslope and base-normal positions of the particles (m)
863	\mathbf{Y}	Fitting parameter for Josserand et al. [2004]’s mean velocity profiles (m)
864	$\dot{\gamma}$	Shear rate (s^{-1})
865	γ_g	Characteristic attenuation coefficient of acoustic energy in granular media (m^{-1})
866	γ_p	Attenuation coefficient of acoustic energy in the basal plate (m^{-1})
867	Δt	Duration (s)
868	$\delta V_x^2, \delta V_y^2$	Variances of grains’ velocity components, within each layer ($\text{m}^2 \text{ s}^{-2}$)
869	$\delta \mathbf{V}, \delta \mathbf{V}_s, \langle \delta \mathbf{V} \rangle$	Local, surficial and depth-averaged RMS fluctuating velocity (m s^{-1})
870	θ	Slope angle ($^\circ$)
871	ν	Poisson’s ratio of the grains’ material ($-$)
872	ξ	Proportion of kinetic energy converted to acoustic energy in a collision ($-$)
873	Π_{el}	Radiated elastic power (J s^{-1})
874	Π_{el}^{Hertz}	Analytical radiated elastic power (J s^{-1})
875	Π_k	Available kinetic power (J s^{-1})
876	ρ, ρ_p	Densities of the grains and the basal plate (kg m^{-3})
877	τ_i, τ	Empirical periods of a particle’s oscillations and their median (s)
878	ϕ	Volumetric packing fraction ($-$)
879	ϕ_{2D}	Surface packing fraction at the side wall ($-$)

880 7 Acknowledgments

881 We thank Xiaoping Jia, Sylvain Viroulet, Diego Berzi and Alexandre Valance for
882 insightful discussions on granular temperature and kinetic theory. We thank Göran Ek-
883 ström for sharing the inverted force history for the Mt Dall, Mt Lituya, Sheemahant Glacier

884 and Lamplughr Glacier landslides. We thank Alain Steyer for his great help in mount-
 885 ing the setup. This work has been mainly funded by the contract ERC-CG-2013-PE10-
 886 617472 SLIDEQUAKE. RT acknowledges the support of the INSU ALEAS and the France-
 887 Norway IRP D-FFRACT programs, and of the Research Council of Norway through
 888 its Centres of Excellence funding scheme, Project No. 262644. MIA acknowledges the
 889 support of the Georgetown Environmental Justice Program.

890 **8 Data Availability Statement**

891 The experimental data and scripts used in this article are available at [Bachelet et
 892 al., 2020].

893 **Appendix A Heights of the Flows**

894 The flow height is measured by detecting the boundaries of particles at the free sur-
 895 face of the flow, in each frame captured by the high-speed camera (Fig. A1a). Then, the
 896 spatial and temporal height profile obtained by repeating the procedure for all instants
 897 (Fig. A1b) is averaged over time (Fig. A1c) and space (Fig. A1d).

902 **Appendix B Velocity Fluctuation Measurements: Window Effect**

903 The estimate of total velocity fluctuations depends on the width w of the window
 904 considered:

$$\delta V^2(y, t) = \frac{1}{w} \int_{y-w/2}^{y+w/2} (\mathbf{V}(y', t) - \langle \mathbf{V} \rangle(y, t))^2 dy', \quad (\text{B1})$$

905 where $\langle \mathbf{V} \rangle(y, t)$ is the average velocity in the center of the box. Since the average ver-
 906 tical velocity equals zero, a first order expansion is $\langle \mathbf{V} \rangle(y, t) = \langle \mathbf{V} \rangle(y', t) - \dot{\gamma}(y)(y' -$
 907 $y)\mathbf{e}_x$, giving:

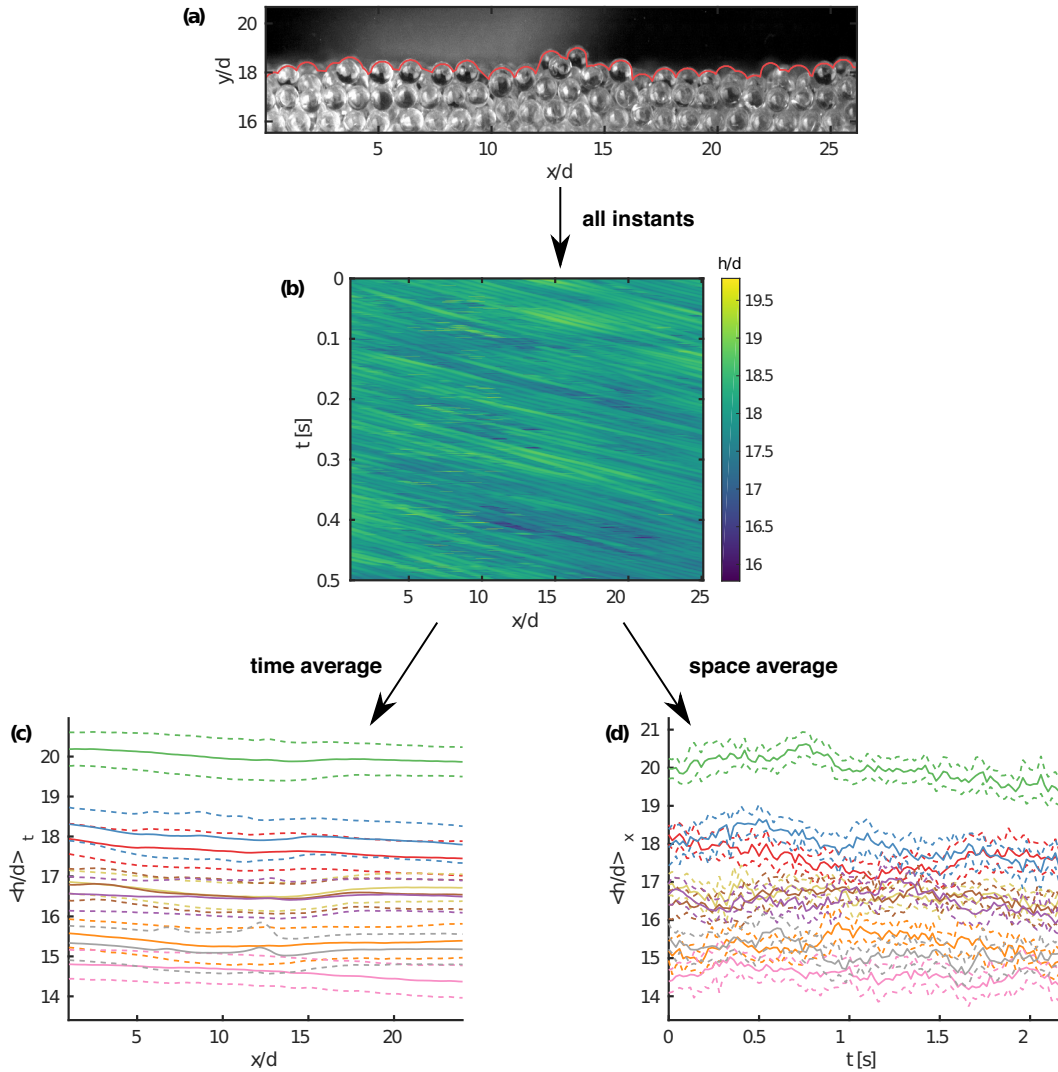
$$\delta V^2(y, t) = \frac{1}{w} \int_{y-w/2}^{y+w/2} (\delta \mathbf{V}^*(y') + \dot{\gamma}(y)(y' - y)\mathbf{e}_x)^2 dy', \quad (\text{B2})$$

908 with $\delta \mathbf{V}^*(y') = \mathbf{V}(y', t) - \langle \mathbf{V} \rangle(y', t)$. Expanding the square leads to three terms I_1 ,
 909 I_2 and I_3 :

$$I_1 = \delta V^{*2}(y, t) = \frac{1}{w} \int_{y-w/2}^{y+w/2} \delta \mathbf{V}^{*2}(y') dy', \quad (\text{B3})$$

$$I_2 = \frac{2}{w} \int_{y-w/2}^{y+w/2} \dot{\gamma}(y)(y' - y) \delta V_x(y') dy', \quad (\text{B4})$$

$$I_3 = \frac{1}{w} \int_{y-w/2}^{y+w/2} (\dot{\gamma}(y)(y' - y))^2 dy' = \frac{w^2 \dot{\gamma}^2(y)}{12}. \quad (\text{B5})$$



898 **Figure A1.** Heights of the flows: (a) example of flow interface detection (red line), (b) space
 899 and time height, thereafter averaged over (c) time or (d) space. Each color of panels (c) and (d)
 900 corresponds to a specific flow (see for example Fig. 11 for detailed legend), while continuous lines
 901 correspond to mean values and dashed lines to one standard deviation either side of these means.

912 I_1 corresponds to the genuine mean of velocity fluctuations at each point. I_2 can be com-
 913 puted by a first order expansion of $\delta V_x(y')$:

$$\delta V_x(y') = \delta V_x(y) + \frac{d\delta V_x}{dy}(y)(y' - y). \quad (\text{B6})$$

914 Thus:

$$I_2 = \frac{2}{w} \left(\delta V_x(y) \int_{y-w/2}^{y+w/2} (y' - y) dy' + \frac{d\delta V_x}{dy}(y) \int_{y-w/2}^{y+w/2} (y' - y)^2 dy' \right). \quad (\text{B7})$$

915 The first term equals zero, whereas the second can be neglected because of the second
 916 order.

917 Finally, total velocity fluctuations estimate are given by the following expression:

$$\delta V^2(y, t) = \delta V^{*2}(y, t) + \frac{w^2 \dot{\gamma}^2(y)}{12}. \quad (\text{B8})$$

918 The second term quantifies the error introduced by considering the average velocity taken
 919 in y (the center of the box) instead of the value in y' in formula (B1). Its expression is
 920 very similar to the one found by Weinhart et al. [2013] (Eq. (34)). The only difference
 921 comes from the choice of the averaging function, also called the coarse-graining function.
 922 We implicitly chose a gate equal to one in $[y-w/2, y+w/2]$ and to zero elsewhere, whereas
 923 a more complex choice is usually selected for differentiability [Glasser & Goldhirsch, 2001,
 924 Weinhart et al., 2013].

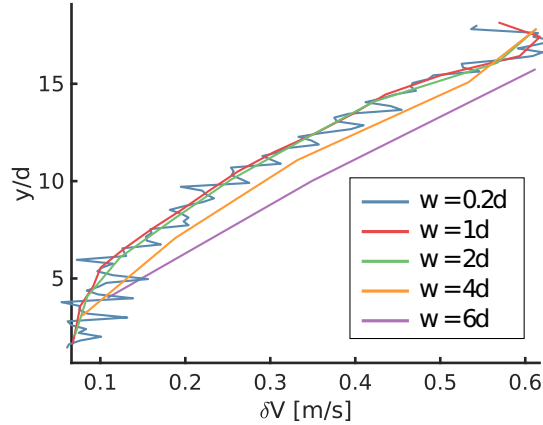
925 Thanks to expression (B8) and approximating δV^* by $2.1 d \dot{\gamma}$, as suggested by the
 926 linear fit in Fig. 7e, it is possible to deduce that the windows have an effect similar to
 927 that of δV^* when $w = 5d$. For this reason, the window is negligible in our case (see Fig.
 928 B1)

930 **Appendix C Correlation Lengths within the Flow**

931 To obtain quantitative measurements of the correlation length of velocity fluctu-
 932 ations we compute the downslope and vertical velocity correlations between two points
 933 M_1 and M_2 with coordinates (x_1, y_1) and (x_2, y_2) :

$$C_{V_i}(M_1, M_2) = \frac{\sum_t \delta V_i(M_1, t) \times \delta V_i(M_2, t)}{\sqrt{\sum_t \delta V_i(M_1, t)^2} \times \sqrt{\sum_t \delta V_i(M_2, t)^2}}, \quad (\text{C1})$$

934 where $i = x, y$. Examples of downslope and vertical velocity correlations are presented
 935 in Figs. C2(a) and (b) respectively. High correlations of the horizontal velocity over one
 936 particle thickness are clearly visible. To quantify this correlation, a correlation length
 937 has been defined. It corresponds to the length at which the correlation reaches a given



929

Figure B1. Effect of the window size on the fluctuation velocity computation.

938

threshold. Unlike Pouliquen [2004] who chose a threshold of 0.05, we selected a value of
 939 0.5 because of the limitation of the window of observation (see the dark grey contour plot
 940 of Fig. C2a which seems cropped by the right border of the window). The correlation
 941 length increases with decreasing slope angle as observed by Pouliquen [2004] and Staron
 942 [2008] or in granular flows approaching jamming [Gardel et al., 2009]. In our experiments,
 943 only the lengths of downslope velocities in the x -direction λ_{xx} are higher than one par-
 944 ticle diameter. This suggests correlated motion of particles of the same layer, support-
 945 ing the layering observed in Fig. 3b. In agreement with Pouliquen [2004] and Staron [2008],
 946 correlation lengths decrease for increasing slope angles (Fig. C2c-e), as observed in Movies
 947 3 and 4 (supplementary material). The correlation lengths collapse to zero under $y/d =$
 948 5 because particle velocities are smaller than noise.

949

Note that for dry granular chute flows [Gardel et al., 2009] and for granular flows
 950 in a fluid [Orpe & Kudrolli, 2007], significantly greater spatial correlations are observed
 951 near the boundaries, which may be the case here.

958

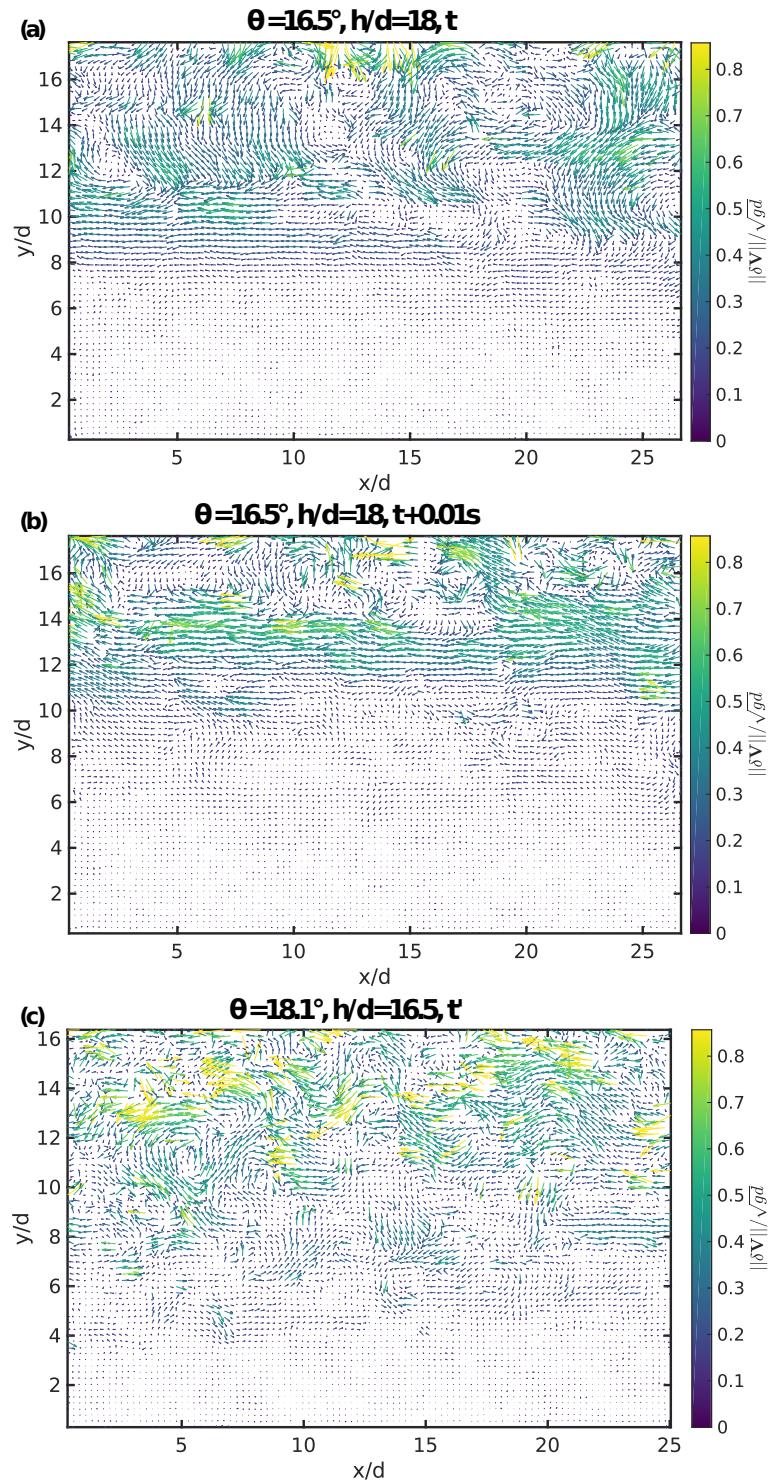
References

959

Akay, A. (2002). Acoustics of friction. *The Journal of the Acoustical Society of*
 960 *America*, 111(4), 1525–1548.

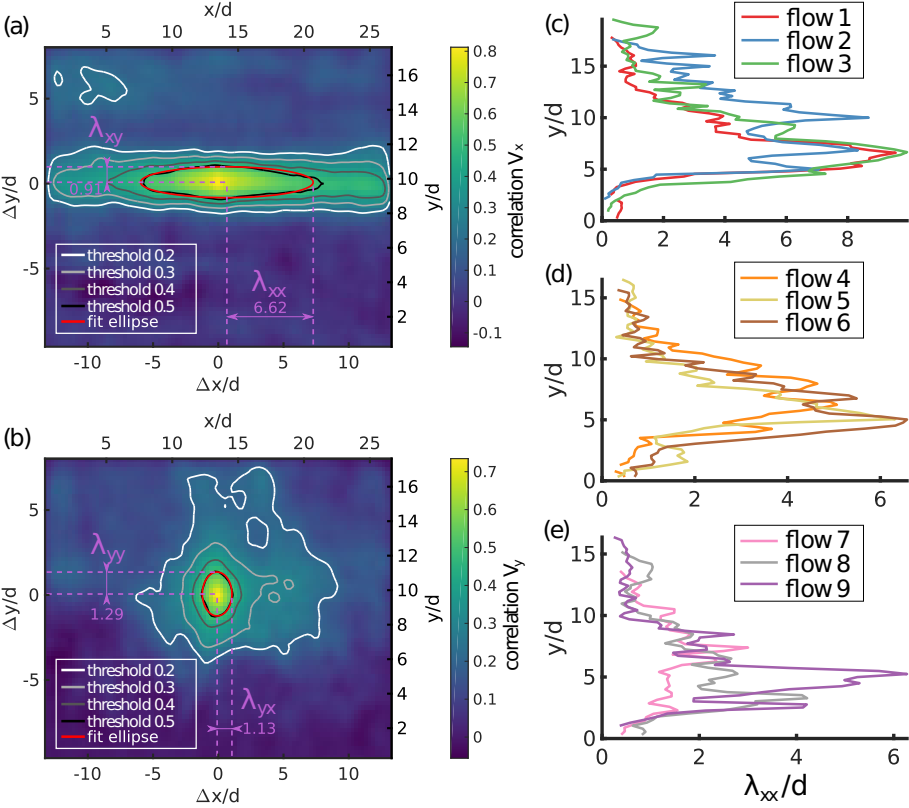
961

Allstadt, K. (2013). Extracting source characteristics and dynamics of the august
 962 2010 mount meager landslide from broadband seismograms. *Journal of Geophys-*
 963 *ical Research: Earth Surface*, 118(3), 1472–1490. Retrieved from <http://dx.doi>



952 **Figure C1.** Map of velocity fluctuations obtained with CIV for flow number 2 (a,b) and 9 (c)

953 at instants t , $t + 0.01s$ and t' respectively (t and t' are arbitrary).



954 **Figure C2.** Example of spatial correlations between the (a) downslope and (b) base-normal
 955 components of fluctuating grain velocities, between the static point of coordinates ($x/d = 14$,
 956 $y/d = 10$) and all the others positions for the flow 2. Panels (c) to (e) correspond to the correla-
 957 tion length λ_{xx} of the horizontal velocity in x direction for all the flows.

- 964 .org/10.1002/jgrf.20110 doi: 10.1002/jgrf.20110
- 965 Allstadt, K., Matoza, R., Lockhart, A., Moran, S., Caplan-Auerbach, J., Haney,
966 M., ... Malone, S. (2018). Seismic and acoustic signatures of surficial mass
967 movements at volcanoes. *Journal of Volcanology and Geothermal Research*, *364*,
968 76-106. doi: 10.1016/j.jvolgeores.2018.09.007
- 969 Allstadt, K. E., Farin, M., Iverson, R. M., Obryk, M. K., Kean, J. W., Tsai,
970 V. C., ... Logan, M. (2020). Measuring basal force fluctuations of debris
971 flows using seismic recordings and empirical green's functions. *Journal of Geo-*
972 *physical Research: Earth Surface*, *125*(9), e2020JF005590. Retrieved from
973 <https://agupubs.onlinelibrary.wiley.com/doi/abs/10.1029/2020JF005590>
974 (e2020JF005590 2020JF005590) doi: 10.1029/2020JF005590
- 975 Ancy, C. (2001). Dry granular flows down an inclined channel: Experimental inves-
976 tigation on the frictional-collisional regime. *Physical Review E*, *65*, 011304. Re-
977 trieved from <https://link.aps.org/doi/10.1103/PhysRevE.65.011304> doi: 10
978 .1103/PhysRevE.65.011304
- 979 Andreotti, B. (2004). The song of dunes as a wave-particle mode locking. *Phys. Rev.*
980 *Lett.*, *93*, 238001. doi: 10.1103/PhysRevLett.93.238001
- 981 Andreotti, B. (2012). Sonic sands. *Reports on Progress in Physics*, *75*(2), 026602.
- 982 Andreotti, B., Forterre, Y., & Pouliquen, O. (2013). *Granular media. between fluid*
983 *and solid*. doi: 10.1017/CBO9781139541008
- 984 Arran, M., Mangeney, A., de Rosny, J., Farin, M., Toussaint, R., & Roche, O.
985 (2021). Laboratory landquakes: Insights from experiments into the high-frequency
986 seismic signal generated by geophysical granular flows. *Journal of Geophysical*
987 *Research - Earth Surface*, *126*(5), e2021JF00617. doi: 10.1029/2021JF006172
- 988 Artoni, R., & Richard, P. (2015a). Average balance equations, scale dependence, and
989 energy cascade for granular materials. *Physical Review E*, *91*(3), 032202.
- 990 Artoni, R., & Richard, P. (2015b). Effective wall friction in wall-bounded 3d dense
991 granular flows. *Physical review letters*, *115*(15), 158001.
- 992 Bachelet, V. (2018). *Étude expérimentale des émissions acoustiques générées par les*
993 *écoulements granulaires* (Unpublished doctoral dissertation). Institut de Physique
994 du Globe de Paris.
- 995 Bachelet, V., Mangeney, A., de Rosny, J., Toussaint, R., & Farin, M. (2018). Elastic
996 wave generated by granular impact on rough and erodible surfaces. *Journal of Ap-*

- 1000 *plied Physics*, 123(4). doi: 10.1063/1.5012979
- 1001 Bachelet, V., Mangeney, A., de Rosny, J., Toussaint, R., Farin, M. , & Hibert,
1002 C. (2020). Stationary granular flow seismicity and optics. *Zenodo*. doi:
1003 10.5281/zenodo.3600306
- 1004 Berzi, D. (2014). Extended kinetic theory applied to dense, granular, simple shear
1005 flows. *Acta Mechanica*, 225(8), 2191–2198.
- 1006 Berzi, D., & Jenkins, J. T. (2011). Surface flows of inelastic spheres. *Physics of Flu-*
1007 *ids*, 23(1), 013303. Retrieved from <http://dx.doi.org/10.1063/1.3532838> doi:
1008 10.1063/1.3532838
- 1009 Bonneau, L., Andreotti, B., & Clément, E. (2008). Evidence of rayleigh-hertz sur-
1010 face waves and shear stiffness anomaly in granular media. *Physical Review Letters*,
1011 101(11), 118001.
- 1012 Calder, E. S., Cortés, J. A., Palma, J. L., & Lockett, R. (2005). Probabilistic anal-
1013 ysis of rockfall frequencies during an andesite lava dome eruption: The soufrière
1014 hills volcano, montserrat. *Geophysical Research Letters*, 32(16), n/a–n/a. Re-
1015 trieved from <http://dx.doi.org/10.1029/2005GL023594> (L16309) doi:
1016 10.1029/2005GL023594
- 1017 Chrzaszcz, K. (2016). *Ondes dans les milieux granulaires: de l'échelle microscopique*
1018 *à l'échelle macroscopique*. (Unpublished doctoral dissertation). Université Paris-
1019 Saclay (ComUE).
- 1020 Courrech du Pont, S., Gondret, P., Perrin, B., & Rabaud, M. (2003). Wall effects on
1021 granular heap stability. *Europhysics Letters*, 61(4), 492. Retrieved from [http://](http://stacks.iop.org/0295-5075/61/i=4/a=492)
1022 stacks.iop.org/0295-5075/61/i=4/a=492 doi: 10.1209/epl/i2003-00156-5
- 1023 Dammeier, F., Moore, J. R., Haslinger, F., & Loew, S. (2011). Characteriza-
1024 tion of alpine rockslides using statistical analysis of seismic signals. *Journal*
1025 *of Geophysical Research: Earth Surface*, 116(F4), n/a–n/a. (F04024) doi:
1026 10.1029/2011JF002037
- 1027 de Haas, T., Åberg, A. S., Walter, F., & Zhang, Z. (2021). Deciphering seismic and
1028 normal-force fluctuation signatures of debris flows: An experimental assessment of
1029 effects of flow composition and dynamics. *Earth Surface Processes and Landforms*,
46(11), 2195–2210. Retrieved from [https://onlinelibrary.wiley.com/doi/](https://onlinelibrary.wiley.com/doi/abs/10.1002/esp.5168)
abs/10.1002/esp.5168 doi: 10.1002/esp.5168
- Delannay, R., Valance, A., Mangeney, A., Roche, O., & Richard, P. (2017). Granular

1030 and particle-laden flows: from laboratory experiments to field observations. *Jour-*
 1031 *nal of Physics D: Applied Physics*, 50(5), 053001. Retrieved from [http://stacks](http://stacks.iop.org/0022-3727/50/i=5/a=053001)
 1032 [.iop.org/0022-3727/50/i=5/a=053001](http://stacks.iop.org/0022-3727/50/i=5/a=053001)

1033 Deparis, J., Jongmans, D., Cotton, F., Baillet, L., Thouvenot, F., & Hantz, D.
 1034 (2008). Analysis of rock-fall and rock-fall avalanche seismograms in the french
 1035 alps. *Bulletin of the Seismological Society of America*, 98(4), 1781. doi:
 1036 10.1785/0120070082

1037 Durand, V., Mangeney, A., Haas, F., Jia, X., Bonilla, F., Peltier, A., ... others
 1038 (2018). On the link between external forcings and slope instabilities in the piton
 1039 de la fournaise summit crater, reunion island. *Journal of Geophysical Research:*
 1040 *Earth Surface*, 123(10), 2422–2442.

1041 Ekström, G., & Stark, C. P. (2013). Simple scaling of catastrophic landslide dynam-
 1042 ics. *Science*, 339(6126), 1416–1419. Retrieved from [http://science.sciencemag](http://science.sciencemag.org/content/339/6126/1416)
 1043 [.org/content/339/6126/1416](http://science.sciencemag.org/content/339/6126/1416) doi: 10.1126/science.1232887

1044 Farin, M., Mangeney, A., de Rosny, J., Toussaint, R., Sainte-Marie, J., & Shapiro,
 1045 N. M. (2016). Experimental validation of theoretical methods to estimate the en-
 1046 ergy radiated by elastic waves during an impact. *Journal of Sound and Vibration*,
 1047 362(Supplement C), 176 - 202. doi: 10.1016/j.jsv.2015.10.003

1048 Farin, M., Mangeney, A., de Rosny, J., Toussaint, R., & Trinh, P.-T. (2018). Link
 1049 between the dynamics of granular flows and the generated seismic signal: Insights
 1050 from laboratory experiments. *Journal of Geophysical Research: Earth Surface*,
 1051 123(6), 1407-1429. doi: 10.1029/2017JF004296

1052 Farin, M., Mangeney, A., de Rosny, J., Toussaint, R., & Trinh, P.-T. (2019). Re-
 1053 lations between the characteristics of granular column collapses and that of the
 1054 generated high-frequency seismic signal. *Journal of Geophysical Research: Earth*
 1055 *Surface*, in press.

1056 Farin, M., Tsai, V. C., Lamb, M. P., & Allstadt, K. E. (2019). A physical model
 1057 of the high-frequency seismic signal generated by debris flows. *Earth Sur-*
 1058 *face Processes and Landforms*, 44(13), 2529–2543. Retrieved from [https://](https://onlinelibrary.wiley.com/doi/abs/10.1002/esp.4677)
 1059 onlinelibrary.wiley.com/doi/abs/10.1002/esp.4677 doi: 10.1002/esp.4677

1060 Farin, M., Mangeney, A., Toussaint, R., de Rosny, J., Shapiro, N. M., Dewez, T., ...
 1061 Berger, F. (2015). Characterization of rockfalls from seismic signal: Insights from
 1062 laboratory experiments. *Journal of Geophysical Research: Solid Earth*, 120(10),

- 1063 7102–7137. (2015JB012331) doi: 10.1002/2015JB012331
- 1064 Favreau, P., Mangeney, A., Lucas, A., Crosta, G., & Bouchut, F. (2010). Numerical
1065 cal modeling of landquakes. *Geophysical Research Letters*, *37*(15), n/a–n/a. Re-
1066 trieved from <http://dx.doi.org/10.1029/2010GL043512> (L15305) doi: 10
1067 .1029/2010GL043512
- 1068 Fernández-Nieto, E. D., Garres-Díaz, J., Mangeney, A., & Narbona-Reina, G.
1069 (2018). 2d granular flows with the μ (i) rheology and side walls friction: A
1070 well-balanced multilayer discretization. *Journal of Computational Physics*, *356*,
1071 192–219.
- 1072 Gardel, E., Sitaridou, E., Facto, K., Keene, E., Hattam, K., Easwar, N., &
1073 Menon, N. (2009). Dynamical fluctuations in dense granular flows. *Philoso-
1074 sophical Transactions of the Royal Society of London A: Mathematical,
1075 Physical and Engineering Sciences*, *367*(1909), 5109–5121. Retrieved from
1076 <http://rsta.royalsocietypublishing.org/content/367/1909/5109> doi:
1077 10.1098/rsta.2009.0189
- 1078 Gimbert, F., Tsai, V., & Lamb, M. (2014). A physical model for seismic noise gen-
1079 eration by turbulent flow in rivers. *J. Geophys. Res.: Earth Surf.*, *119*, 2209–2238.
1080 doi: 10.1007/s10035-017-0738-1
- 1081 Glasser, B. J., & Goldhirsch, I. (2001). Scale dependence, correlations, and fluctu-
1082 ations of stresses in rapid granular flows. *Physics of Fluids*, *13*(2), 407–420. Re-
1083 trieved from <https://doi.org/10.1063/1.1338543> doi: 10.1063/1.1338543
- 1084 Goldhirsch, I. (2008). Introduction to granular temperature. *Powder Technology*,
1085 *182*(2), 130 - 136. (Granular Temperature) doi: [https://doi.org/10.1016/j.powtec](https://doi.org/10.1016/j.powtec.2007.12.002)
1086 .2007.12.002
- 1087 Gollin, D., Berzi, D., & Bowman, E. T. (2017). Extended kinetic theory applied to
1088 inclined granular flows: role of boundaries. *Granular Matter*, *19*(3), 56.
- 1089 Gollin, D., Bowman, E., & Shepley, P. (2015a). Granular temperature measurements
1090 of uniform granular flows. In *Deformation characteristics of geomaterials*. doi: 10
1091 .3233/978-1-61499-601-9-647
- 1092 Gollin, D., Bowman, E., & Shepley, P. (2015b). Methods for the physical measure-
1093 ment of collisional particle flows. In *Iop conference series: Earth and environmen-
1094 tal science* (Vol. 26, p. 012017). doi: 10.1088/1755-1315/26/1/012017
- 1095 Hanes, D., & Walton, O. (2000). Simulations and physical measurements of

- 1096 glass spheres flowing down a bumpy incline. *Powder Technology*, 109(1), 133 -
 1097 144. Retrieved from [http://www.sciencedirect.com/science/article/pii/](http://www.sciencedirect.com/science/article/pii/S0032591099002326)
 1098 [S0032591099002326](http://www.sciencedirect.com/science/article/pii/S0032591099002326) doi: 10.1016/S0032-5910(99)00232-6
- 1099 Hibert, C., Ekström, G., & Stark, C. (2017b). The relationship between bulk-mass
 1100 momentum and short-period seismic radiation in catastrophic landslides. *J. Geo-*
 1101 *phys. Res. Earth Surface*, 122, 1201–1215. doi: doi.org/10.1002/2016JF004027
- 1102 Hibert, C., Malet, J.-P., Bourrier, F., Provost, F., Berger, F., Bornemann, P., ...
 1103 Mermin, E. (2017c). Single-block rockfall dynamics inferred from seismic signal
 1104 analysis. *Earth Surface Dynamics*, 5(2), 283. doi: 10.5194/esurf-5-283-2017
- 1105 Hibert, C., Mangeney, A., Grandjean, G., Baillard, C., Rivet, D., Shapiro, N. M., ...
 1106 Crawford, W. (2014). Automated identification, location, and volume estimation
 1107 of rockfalls at piton de la fournaise volcano. *Journal of Geophysical Research:*
 1108 *Earth Surface*, 119(5), 1082–1105. doi: 10.1002/2013JF002970
- 1109 Hibert, C., Mangeney, A., Grandjean, G., Peltier, A., DiMuro, A., Shapiro, N. M.,
 1110 ... Kowalski, P. (2017a). Spatio-temporal evolution of rockfall activity from 2007
 1111 to 2011 at the piton de la fournaise volcano inferred from seismic data. *Jour-*
 1112 *nal of Volcanology and Geothermal Research*, 333(Supplement C), 36 - 52. doi:
 1113 10.1016/j.jvolgeores.2017.01.007
- 1114 Hibert, C., Mangeney, A., Grandjean, G., & Shapiro, N. M. (2011). Slope insta-
 1115 bilities in dolomieu crater, réunion island: From seismic signals to rockfall char-
 1116 acteristics. *Journal of Geophysical Research: Earth Surface*, 116(F4), n/a–n/a.
 1117 (F04032) doi: 10.1029/2011JF002038
- 1118 Hill, K. M., & Tan, D. S. (2014). Segregation in dense sheared flows: gravity, tem-
 1119 perature gradients, and stress partitioning. *Journal of Fluid Mechanics*, 756, 54–
 1120 88.
- 1121 Hostler, S. R. (2004). *Wave propagation in granular materials* (Unpublished doc-
 1122 toral dissertation). California Institute of Technology.
- 1123 Hostler, S. R., & Brennen, C. E. (2005, Sep). Pressure wave propagation in a granu-
 1124 lar bed. *Physical Review E*, 72, 031303. Retrieved from [https://link.aps.org/](https://link.aps.org/doi/10.1103/PhysRevE.72.031303)
 1125 [doi/10.1103/PhysRevE.72.031303](https://link.aps.org/doi/10.1103/PhysRevE.72.031303) doi: 10.1103/PhysRevE.72.031303
- 1126 Huang, C.-J., Shieh, C.-L., & Yin, H.-Y. (2004). Laboratory study of the un-
 1127 derground sound generated by debris flows. *Journal of Geophysical Research:*
 1128 *Earth Surface*, 109(F1), n/a–n/a. Retrieved from <http://dx.doi.org/10.1029/>

- 1129 2003JF000048 (F01008) doi: 10.1029/2003JF000048
- 1130 Huang, C.-J., Yin, H.-Y., Chen, C.-Y., Yeh, C.-H., & Wang, C.-L. (2007). Ground
1131 vibrations produced by rock motions and debris flows. *Journal of Geophysical Re-*
1132 *search: Earth Surface*, 112(F2), n/a–n/a. Retrieved from <http://dx.doi.org/10>
1133 [.1029/2005JF000437](http://dx.doi.org/10.1029/2005JF000437) (F02014) doi: 10.1029/2005JF000437
- 1134 Hunt, M. L., & Vriend, N. M. (2010). Booming sand dunes. *Annual Re-*
1135 *view of Earth and Planetary Sciences*, 38(1), 281–301. Retrieved from
1136 <https://doi.org/10.1146/annurev-earth-040809-152336> doi: 10.1146/
1137 annurev-earth-040809-152336
- 1138 Johnson, K. L. (1987). *Contact mechanics*. Cambridge university press. doi: 10
1139 [.1017/CBO9781139171731](https://doi.org/10.1017/CBO9781139171731)
- 1140 Jop, P., Forterre, Y., & Pouliquen, O. (2005). Crucial role of sidewalls in granu-
1141 lar surface flows: consequences for the rheology. *Journal of Fluid Mechanics*, 541,
1142 167–192. doi: 10.1017/S0022112005005987
- 1143 Jop, P., Forterre, Y., & Pouliquen, O. (2007). Initiation of granular surface flows in
1144 a narrow channel. *Physics of Fluids*, 19(8), 088102. Retrieved from <http://dx>
1145 [.doi.org/10.1063/1.2753111](http://dx.doi.org/10.1063/1.2753111) doi: 10.1063/1.2753111
- 1146 Josserand, C., Lagrée, P.-Y., & Lhuillier, D. (2004). Stationary shear flows of dense
1147 granular materials: a tentative continuum modelling. *The European Physical Jour-*
1148 *nal E*, 14(2), 127–135. Retrieved from <https://doi.org/10.1140/epje/i2003>
1149 [-10141-4](https://doi.org/10.1140/epje/i2003-10141-4) doi: 10.1140/epje/i2003-10141-4
- 1150 Kanamori, H., & Given, J. W. (1982). Analysis of long-period seismic waves excited
1151 by the may 18, 1980, eruption of mount st. helens—a terrestrial monopole? *Jour-*
1152 *nal of Geophysical Research: Solid Earth*, 87(B7), 5422–5432.
- 1153 Kean, J. W., Coe, J. A., Coviello, V., Smith, J. B., McCoy, S. W., & Arattano,
1154 M. (2015). Estimating rates of debris flow entrainment from ground vi-
1155 brations. *Geophysical Research Letters*, 42(15), 6365–6372. Retrieved from
1156 <https://agupubs.onlinelibrary.wiley.com/doi/abs/10.1002/2015GL064811>
1157 doi: 10.1002/2015GL064811
- 1158 Kharel, P., & Rognon, P. (2017). Vortices enhance diffusion in dense granular flows.
1159 *Physical Review Letters*, 119, 178001. Retrieved from <https://link.aps.org/>
1160 [doi/10.1103/PhysRevLett.119.178001](https://doi.org/10.1103/PhysRevLett.119.178001) doi: 10.1103/PhysRevLett.119.178001
- 1161 Kolmogorov, A. (1941). The local structure of turbulence in incompressible viscous

- 1162 fluid for very large reynolds numbers. *Akad. Nauk SSSR Dokl.*, *30*, 301–305.
- 1163 Kuehnert, J., Mangeney, A., Capdeville, Y., Métaxian, J. P., Bonilla, L. F., Stutz-
 1164 mann, E., ... Hibert, C. (2020). Simulation of topography effects on rockfall-
 1165 generated seismic signals: Application to piton de la fournaise volcano. *Journal*
 1166 *of Geophysical Research: Solid Earth*, *125*(10), e2020JB019874. Retrieved from
 1167 <https://agupubs.onlinelibrary.wiley.com/doi/abs/10.1029/2020JB019874>
 1168 (e2020JB019874 10.1029/2020JB019874) doi: 10.1029/2020JB019874
- 1169 Kuehnert, J., Mangeney, A., Capdeville, Y., Vilotte, J. P., Stutzmann, E., Chaljub,
 1170 E., ... Lauret, F. (2021). Locating rockfalls using inter-station ratios of seis-
 1171 mic energy at dolomieu crater, piton de la fournaise volcano. *Journal of Geo-*
 1172 *physical Research: Earth Surface*, *126*(4), e2020JF005715. Retrieved from
 1173 <https://agupubs.onlinelibrary.wiley.com/doi/abs/10.1029/2020JF005715>
 1174 (e2020JF005715 2020JF005715) doi: 10.1029/2020JF005715
- 1175 La Rocca, M., Galluzzo, D., Saccorotti, G., Tinti, S., Cimini, G. B., & Del Pezzo, E.
 1176 (2004). Seismic signals associated with landslides and with a tsunami at stromboli
 1177 volcano, italy. *Bulletin of the Seismological Society of America*, *94*(5), 1850. Re-
 1178 trieved from <http://dx.doi.org/10.1785/012003238> doi: 10.1785/012003238
- 1179 Lai, V. H., Tsai, V. C., Lamb, M. P., Ulizio, T. P., & Beer, A. R. (2018, 06).
 1180 The seismic signature of debris flows: Flow mechanics and early warning at
 1181 montecito, california. *Geophysical Research Letters*, *45*(11), p5528–5535. doi:
 1182 10.1029/2018GL077683
- 1183 Leclercq, M., Picart, P., Penelet, G., & Tournat, V. (2017). Investigation of 3d
 1184 surface acoustic waves in granular media with 3-color digital holography. *J. Appl.*
 1185 *Phys.*, *121*, 045112. doi: 10.1063/1.4974950
- 1186 Legland, J.-B., Tournat, V., Dazel, O., & Novak, A. (2012). Linear and nonlinear
 1187 biot waves in a noncohesive granular medium slab: transfer function, self-action,
 1188 second harmonic generation. *J. Acoust. Soc. Am.*, *113*(6), 4292–4303.
- 1189 Levy, C., Mangeney, A., Bonilla, F., Hibert, C., Calder, E. S., & Smith, P. J. (2015).
 1190 Friction weakening in granular flows deduced from seismic records at the soufrière
 1191 hills volcano, montserrat. *Journal of Geophysical Research: Solid Earth*, *120*(11),
 1192 7536–7557. doi: 10.1002/2015JB012151
- 1193 Lherminier, S., Planet, R., Simon, G., Vanel, L., & Ramos, O. (2014). Revealing the
 1194 structure of a granular medium through ballistic sound propagation. *Phys. Rev.*

- 1195 *Lett.*, 113(9), 098001.
- 1196 Lin, Y.-N., Sieh, K., & Stock, J. (2010). Submarine landslides along the malacca
1197 strait-mergui basin shelf margin: Insights from sequence-stratigraphic anal-
1198 ysis. *Journal of Geophysical Research: Solid Earth*, 115(12). doi: 10.1029/
1199 2009JB007050
- 1200 Liu, C.-h., & Nagel, S. R. (1993). Sound in a granular material: disorder and nonlin-
1201 earity. *Physical Review B*, 48(21), 15646.
- 1202 Lucas, A., Mangeney, A., & Ampuero, J.-P. (2014). Frictional velocity-weakening
1203 in landslides on earth and on other planetary bodies. *Nature Communications*, 5,
1204 3417. Retrieved from <http://dx.doi.org/10.1038/ncomms4417> doi: 10.1038/
1205 ncomms4417
- 1206 Mandal, S., & Khakhar, D. V. (2017). A sidewall friction driven ordering transi-
1207 tion in granular channel flows: Implications for granular rheology. *arXiv preprint*
1208 *arXiv:1706.05503*.
- 1209 Martin, R., Bodet, L., Tournat, V., & Rejiba, F. (2018). Seismic wave propagation
1210 in nonlinear viscoelastic media using the auxiliary differential equation method.
1211 *Geophys. J. Int.*, 216(1), 453-469. doi: 10.1093/gji/ggy441
- 1212 Michlmayr, G., Cohen, D., & Or, D. (2013). Shear-induced force fluctuations
1213 and acoustic emissions in granular material. *Journal of Geophysical Research:*
1214 *Solid Earth*, 118(12), 6086–6098. Retrieved from [http://dx.doi.org/10.1002/](http://dx.doi.org/10.1002/2012JB009987)
1215 [2012JB009987](http://dx.doi.org/10.1002/2012JB009987) doi: 10.1002/2012JB009987
- 1216 GDR MiDi, (2004). On dense granular flows. *The European Physical Journal E*,
1217 14(4), 341–365. Retrieved from <https://doi.org/10.1140/epje/i2003-10153-0>
1218 doi: 10.1140/epje/i2003-10153-0
- 1219 Moretti, L., Mangeney, A., Walter, F. , Capdeville, Y., Bodin, T. , Stutzmann,
1220 E., Huggel, C., Schneider, D., & Le Friant, A. (2020). Numerical model-
1221 ing of the mount steller landslide flow history and of the generated long pe-
1222 riod seismic waves. *Geophysical Research Letters*, 39(16), n/a–n/a. Re-
1223 trieved from <http://dx.doi.org/10.1029/2012GL052511> (L16402) doi:
1224 10.1029/2012GL052511
- 1225 Moretti, L., Allstadt, K., Mangeney, A., Capdeville, Y., Stutzmann, E., & Bouchut,
1226 F. (2015). Numerical modeling of the mount meager landslide constrained by
1227 its force history derived from seismic data. *Journal of Geophysical Research:*

- 1228 *Solid Earth*, 120(4), 2579–2599. Retrieved from <http://dx.doi.org/10.1002/>
 1229 2014JB011426 (2014JB011426) doi: 10.1002/2014JB011426
- 1230 Moretti, L., Mangeney, A., Capdeville, Y., Stutzmann, E., Huggel, C., Schneider, D.,
 1231 & Bouchut, F. (2012). Numerical modeling of the mount steller landslide flow his-
 1232 tory and of the generated long period seismic waves. *Geophysical Research Letters*,
 1233 39(16), n/a–n/a. Retrieved from <http://dx.doi.org/10.1029/2012GL052511>
 1234 (L16402) doi: 10.1029/2012GL052511
- 1235 Mouraille, O., & Luding, S. (2008). Sound wave propagation in weakly polydisperse
 1236 granular materials. *Ultrasonics*, 48(6), 498 - 505. Retrieved from <http://www>
 1237 [.sciencedirect.com/science/article/pii/S0041624X08000462](http://www.sciencedirect.com/science/article/pii/S0041624X08000462) (Selected Pa-
 1238 pers from ICU 2007) doi: 10.1016/j.ultras.2008.03.009
- 1239 Norris, R. D. (1994). Seismicity of rockfalls and avalanches at three cascade range
 1240 volcanoes: Implications for seismic detection of hazardous mass movements.
 1241 *Bulletin of the Seismological Society of America*, 84(6), 1925. Retrieved from
 1242 <http://dx.doi.org/>
- 1243 Okal, E. A. (1990). Single forces and double-couples: a theoretical review of their
 1244 relative efficiency for the excitation of seismic and tsunami waves. *Journal of*
 1245 *Physics of the Earth*, 38(6), 445–474.
- 1246 Okuda, S., Suwa, H., Okunishi, K., Yokoyama, K., & Nakano, M. (1980). Obser-
 1247 vations on the motion of a debris flow and its geomorphological effect. *Z. Geomor-*
 1248 *phol. NF Suppl. Bd.*, 35, 142–163.
- 1249 Orpe, A. V., & Kudrolli, A. (2007). Velocity correlations in dense granular flows ob-
 1250 served with internal imaging. *Physical Review Letters*, 98, 238001. Retrieved from
 1251 <https://link.aps.org/doi/10.1103/PhysRevLett.98.238001> doi: 10.1103/
 1252 PhysRevLett.98.238001
- 1253 Pouliquen, O. (2004). Velocity correlations in dense granular flows. *Physical Re-*
 1254 *view Letters*, 93, 248001. Retrieved from [https://link.aps.org/doi/10.1103/](https://link.aps.org/doi/10.1103/PhysRevLett.93.248001)
 1255 PhysRevLett.93.248001 doi: 10.1103/PhysRevLett.93.248001
- 1256 Royer, D., & Dieulesaint, E. (2000). *Elastic waves in solids i: Free and guided prop-*
 1257 *agation*. Springer Berlin Heidelberg.
- 1258 Sarno, L., Papa, M. N., Villani, P., & Tai, Y.-C. (2016). An optical method for
 1259 measuring the near-wall volume fraction in granular dispersions. *Granular Matter*,
 1260 18(4), 80. doi: 10.1007/s10035-016-0676-3

- 1261 Schneider, D., Bartelt, P., Caplan-Auerbach, J., Christen, M., Huggel, C., &
 1262 McArdell, B. W. (2010). Insights into rock-ice avalanche dynamics by com-
 1263 bined analysis of seismic recordings and a numerical avalanche model. *Journal of*
 1264 *Geophysical Research: Earth Surface*, 115(F4), n/a–n/a. Retrieved from [http://](http://dx.doi.org/10.1029/2010JF001734)
 1265 dx.doi.org/10.1029/2010JF001734 (F04026) doi: 10.1029/2010JF001734
- 1266 Staron, L. (2008). Correlated motion in the bulk of dense granular flows. *Physi-*
 1267 *cal Review E*, 77, 051304. Retrieved from [https://link.aps.org/doi/10.1103/](https://link.aps.org/doi/10.1103/PhysRevE.77.051304)
 1268 [PhysRevE.77.051304](https://link.aps.org/doi/10.1103/PhysRevE.77.051304) doi: 10.1103/PhysRevE.77.051304
- 1269 Taberlet, N., Richard, P., Valance, A., Losert, W., Pasini, J. M., Jenkins, J. T., &
 1270 Delannay, R. (2003). Superstable granular heap in a thin channel. *Physical Re-*
 1271 *view Letters*, 91, 264301. Retrieved from [https://link.aps.org/doi/10.1103/](https://link.aps.org/doi/10.1103/PhysRevLett.91.264301)
 1272 [PhysRevLett.91.264301](https://link.aps.org/doi/10.1103/PhysRevLett.91.264301) doi: 10.1103/PhysRevLett.91.264301
- 1273 Taylor, S., & Brodsky, E. E. (2017). Granular temperature measured experimen-
 1274 tally in a shear flow by acoustic energy. *Physical Review E*, 96, 032913. Retrieved
 1275 from <https://link.aps.org/doi/10.1103/PhysRevE.96.032913> doi: 10.1103/
 1276 [PhysRevE.96.032913](https://link.aps.org/doi/10.1103/PhysRevE.96.032913)
- 1277 Thielicke, W., & Stamhuis, E. (2014). Pivlab—towards user-friendly, affordable and
 1278 accurate digital particle image velocimetry in matlab. *Journal of Open Research*
 1279 *Software*, 2(1). doi: 10.5334/jors.bl
- 1280 van den Wildenberg, S., van Hecke, M., & Jia, X. (2013). Evolution of granular
 1281 packings by nonlinear acoustic waves. *EPL (Europhysics Letters)*, 101(1), 14004.
 1282 Retrieved from <http://stacks.iop.org/0295-5075/101/i=1/a=14004> doi: 10
 1283 [.1209/0295-5075/101/14004](http://stacks.iop.org/0295-5075/101/i=1/a=14004)
- 1284 Voronina, V., & Horoshenkov, K. (2004). Acoustic properties of unconsolidated
 1285 granular mixes. *Applied Acoustics*, 65(7), 673 - 691. Retrieved from [http://www](http://www.sciencedirect.com/science/article/pii/S0003682X03001956)
 1286 [.sciencedirect.com/science/article/pii/S0003682X03001956](http://www.sciencedirect.com/science/article/pii/S0003682X03001956) doi: 10.1016/
 1287 [j.apacoust.2003.12.002](http://www.sciencedirect.com/science/article/pii/S0003682X03001956)
- 1288 Weinhart, T., Hartkamp, R., Thornton, A. R., & Luding, S. (2013). Coarse-grained
 1289 local and objective continuum description of three-dimensional granular flows
 1290 down an inclined surface. *Physics of Fluids*, 25(7), 070605. Retrieved from
 1291 <https://doi.org/10.1063/1.4812809> doi: 10.1063/1.4812809
- 1292 Westerweel, J., & Scarano, F. (2005). Universal outlier detection for piv data.
 1293 *Experiments in Fluids*, 39(6), 1096–1100. Retrieved from <https://doi.org/>

- 1294 10.1007/s00348-005-0016-6 doi: 10.1007/s00348-005-0016-6
- 1295 Yamada, M., Kumagai, H., Matsushi, Y., & Matsuzawa, T. (2013). Dynamic land-
 1296 slide processes revealed by broadband seismic records. *Geophysical Research Let-*
 1297 *ters*, *40*(12), 2998–3002. Retrieved from <http://dx.doi.org/10.1002/grl.50437>
 1298 doi: 10.1002/grl.50437
- 1299 Yamada, M., Mangeney, A., Matsushi, Y., & Matsuzawa, T. (2018). Estimation
 1300 of dynamic friction and movement history of large landslides. *Landslides*, *15*(10),
 1301 1963-1974. doi: 10.1007/s10346-018-1002-4
- 1302 Yamada, M., Mangeney, A., Matsushi, Y., & Moretti, L. (2016). Estima-
 1303 tion of dynamic friction of the akatani landslide from seismic waveform inver-
 1304 sion and numerical simulation. *Geophysical Journal International*, *206*(3),
 1305 1479-1486. Retrieved from <http://dx.doi.org/10.1093/gji/ggw216> doi:
 1306 10.1093/gji/ggw216
- 1307 Zhang, Z., Walter, F., McArdell, B. W., de Haas, T., Wenner, M., Chmiel, M., &
 1308 He, S. (2021). Analyzing bulk flow characteristics of debris flows using their
 1309 high frequency seismic signature. *Journal of Geophysical Research: Solid Earth*,
 1310 *126*(12), e2021JB022755. Retrieved from <https://agupubs.onlinelibrary>
 1311 [.wiley.com/doi/abs/10.1029/2021JB022755](https://agupubs.onlinelibrary.wiley.com/doi/abs/10.1029/2021JB022755) (e2021JB022755 2021JB022755)
 1312 doi: 10.1029/2021JB022755
- 1313 Zhao, J., Moretti, L., Mangeney, A., Stutzmann, E., Kanamori, H., Capdeville, Y.,
 1314 ... LeFriant, A. (2015). Model space exploration for determining landslide source
 1315 history from long-period seismic data. *Pure and Applied Geophysics*, *172*(2),
 1316 389-413. doi: 10.1007/s00024-014-0852-5